

Valid time shifting Ensemble Kalman filter (VTS-EnKF) for dust storm forecasting

Mijie Pang¹, Jianbing Jin¹, Arjo Segers², Huiya Jiang³, Wei Han⁴, Batjargal Buyantogtokh⁵, Ji Xia¹, Li Fang¹, Jiandong Li¹, Hai Xiang Lin^{6,7}, and Hong Liao¹

¹Joint International Research Laboratory of Climate and Environment Change, Jiangsu Key Laboratory of Atmospheric Environment Monitoring and Pollution Control, Jiangsu Collaborative Innovation Center of Atmospheric Environment and Equipment Technology, School of Environmental Science and Engineering, Nanjing University of Information Science and Technology, Nanjing, Jiangsu, China

²TNO, Department of Climate, Air and Sustainability, The Netherlands

³College of Environment and Resources, Nanjing Agricultural University

⁴Numerical Weather Prediction Center, Chinese Meteorological Administration, Beijing, China

⁵Information and Research Institute of Meteorology, Hydrology and Environment, Ulaanbaatar, Mongolia

⁶Delft Institute of Applied Mathematics, Delft University of Technology, Delft, The Netherlands

⁷Institute of Environment Sciences, Leiden University, The Netherlands

Correspondence: Jianbing Jin (jianbing.jin@nuist.edu.cn)

Abstract. Dust storms pose significant risks to health and property, necessitating accurate forecasting for preventive measures. Despite advancements, dust models grapple with uncertainties arising from emission and transport processes. Data assimilation addresses these by integrating observations to rectify model error, enhancing forecast precision. The Ensemble Kalman Filter (EnKF) is a widely-used assimilation algorithm that effectively optimize model states, particularly in terms of intensity adjustment. However, the EnKF's efficacy is challenged by position errors between modeled and observed dust features, especially under substantial position errors. This study introduces the Valid Time Shifting-Ensemble Kalman Filter (VTS-EnKF) which combines stochastic EnKF with a valid time shifting mechanism. By recruiting additional ensemble members from neighboring valid times, this method not only accommodates variations in dust load but also explicitly accounts for positional uncertainties. Consequently, the enlarged ensemble better represents both the intensity and positional errors, thereby optimizing the utilization of observational data. The proposed VTS-EnKF was evaluated against two severe dust storm cases from spring 2021, demonstrating that position errors notably deteriorated forecast performance in terms of Root Mean Square Error (RMSE) and Normalized Mean Bias (NMB), impeding the EnKF's effective assimilation. Conversely, the VTS-EnKF improved both the analysis and forecast accuracy compared to the conventional EnKF. Additionally, to provide a more rigorous assessment of its performance, experiments were conducted using fewer ensemble members and different time intervals.

1 Introduction

Dust storms, identified as natural meteorological disasters, are phenomena closely associated with the prevalence of potent winds over arid regions with a loosely packed soil composition (Zhang et al., 2005; An et al., 2018). These storms enable dust particulates to ascend to remarkable heights, traversing distances of thousands of kilometers, with documented aerosol

concentrations soaring to thousands $\mu\text{g m}^{-3}$ (She et al., 2018). During transportation, these aerosols further participate in heterogeneous chemical reactions with SO_x and NO_x , exacerbating the severity of aerosol pollution (Song et al., 2022), thereby significantly endangering human health through respiratory and circulatory system impairments (Gross et al., 2018; Goudie, 2014). East Asia, a dominant source and recipient of dust activity (Hu et al., 2019), has witnessed intensified scholarly focus. Notably, the spring of 2021 observed the onslaught of several super dust storms—unprecedented in intensity and geographical span over the past decade (Filonchik and Peterson, 2022)—resulting in substantial life and property losses across Mongolia and China (Gui et al., 2022; Jin et al., 2022; Tang et al., 2022). Consequently, the imperative for an accurate and timely forecasting system to dust storms is accentuated, aiming to mitigate their detrimental impacts.

In recent years, heightened public concern has fueled advancements in deciphering the physical mechanisms governing dust cycle dynamics, leading to significant strides since the 1990s. To accurately replicate dust storm behavior, numerous dust emission parameterization schemes have been devised, including MB95 (Marticorena and Bergametti, 1995), Shao96 (Shao et al., 1996; Shao, 2004), Zender03 (Zender et al., 2003), and the more recent K14 (Kok et al., 2014). Integrated within chemical transport models, these frameworks facilitate dust storm modeling exercises, exemplified by systems such as CUACE/DUST (Gong and Zhang, 2008), BSC-DREAM8b (Pérez et al., 2006; Mona et al., 2014), GEOS-Chem (Duncan Fairlie et al., 2007), and LOTOS-EUROS (Timmermans et al., 2017; Manders et al., 2017). These models are instrumental in assessing health hazards, quantifying the planet's ecosystem responses, elucidating large-scale climate drivers, and, importantly, informing the development of early warning systems capable of predicting imminent dust loads within timescales ranging from hours to days. Despite these advancements, the forecast skill of such models remains constrained by inherent uncertainties tied to input variables—such as wind velocity fields and initial/boundary conditions—as well as computational approximations necessitated by coarse spatial and temporal resolutions (Mallet and Sportisse, 2006). Of particular note, the scientific consensus highlights the emission parameterization uncertainty as the paramount source of error in dust storm simulations (Ginoux et al., 2001, 2012; Di Tomaso et al., 2017, 2022; Jin et al., 2019a, b). Consequently, the predictive prowess of numerical dust models is notably compromised under the weight of these combined limitations.

Observational studies constitute another pivotal approach in elucidating the intensity and spatial dispersion of dust storms (Muhammad Akhlaq et al., 2012). Among these, satellite-based monitoring technologies have rapidly evolved into a prevalent tool for dust storm detection, offering expansive and detailed insights (Gui et al., 2022). Platforms like MODIS, Himawari, and Fengyun-4A deliver a wealth of data on aerosol characteristics, characterized by high spatial resolution and global coverage. Nonetheless, these satellite products aggregate column-integrated information and are prone to interference from cloud cover and other atmospheric constituents, thereby introducing substantial uncertainties and biases into dust load estimates. Consequently, preprocessing is imperative to ensure their reliability in depicting actual dust concentrations (Jin et al., 2019b, 2022). Concurrently, ground-based observational networks, known for their reliability and fine temporal resolution, play a crucial role in precisely measuring aerosol concentrations (She et al., 2018). China, in particular, has made substantial investments in constructing its ground monitoring infrastructure, establishing an expansive network comprising over 1,600 stations nationwide. This dense grid of ground stations furnishes a granular view of dust plume dynamics across the region (Gui et al., 2022),

enriching the dataset for examining East Asian dust storms and reinforcing the national observation network's capacity for comprehensive dust research.

55 Data assimilation stands as a potent methodology that harmoniously merges model with observations. Rooted in Bayesian principles, its objective is to ascertain the most plausible model state posterior, given the available observations, through probabilistic estimation (Law and Stuart, 2012). The realm of data assimilation encompasses two principal methodologies: variational techniques and filtering algorithms. Variational methodologies, exemplified by 4DVar, strive to determine an optimal analysis that reconciles both prior knowledge and observational constraints over a defined temporal span, achieved by
60 optimizing a predefined cost function (Rabier and Liu, 2003). These methods are prominently employed in tasks such as inverse modeling for initial conditions and emission fields (Jin et al., 2022; Bergamaschi et al., 2010; Corazza et al., 2011), as well as in reanalysis endeavors. However, their implementation hinges on the often intricate development and maintenance of tangent linear or adjoint model forms. Furthermore, the computational burden associated with minimizing the cost function escalates dramatically with the complexity and dimensionality of the models. Conversely, filtering methodologies assimilate observa-
65 tions sequentially, aligning them favorably with operational forecasting frameworks. This class includes the Kalman Filter (Kalman, 1960), its extension in the Extended Kalman Filter (Brunner et al., 2012), and the more sophisticated Particle Filter (Leeuwen et al., 2019). Prominent among these is the Ensemble Kalman Filter (EnKF), distinguished for its adeptness at managing high-dimensional systems, amenability to parallel computation (Evensen, 1994; Katzfuss et al., 2016; Houtekamer and Zhang, 2016), and reliance on ensemble members to infer background error covariance structures (Hamill, 2006; Houtekamer et al., 2014). Its virtues encompass nonlinearity accommodation, dispensing with the necessity for explicit tangent linear calculations, and computational efficacy (Bannister, 2017), rendering it a favored tool across domains, including weather prediction (Houtekamer et al., 2005) and hydrological studies (Reichle et al., 2002). Despite these strengths, the EnKF, as an extension of the Kalman Filter, presumes Gaussian error distributions (Amezcuca and Van Leeuwen, 2014). When dealing with non-Gaussian error statistics, EnKF can create suboptimal outcomes for the linearized dynamics or operators and sampling errors caused by
75 finite ensemble members (Lei et al., 2010).

Uncertainty in dust storm modeling predominantly stems from the real-time estimation of dust emissions, leading to a research emphasis on emission inversion through data assimilation techniques. Studies such as those conducted by Yumimoto and Takemura (2015) leveraged long-term MODIS Aerosol Optical Depth (AOD) retrievals for emission inversion across Asia. Similarly, Escribano et al. (2017) underscored the varying impact of distinct satellite AOD datasets on emission inversions over
80 northern Africa and the Arabian Peninsula, revealing instances where model uncertainties outweigh observational uncertainties in determining assimilation outcomes. Building upon this foundation, recent investigations have delved deeper into the intricacies of dust emission variability in the Mongolian and Chinese Gobi deserts. This includes the assimilation of ground-level PM₁₀ concentrations (Jin et al., 2018), polar-orbiting MODIS satellite data (Jin et al., 2022), and geostationary Himawari-8 AOD measurements (Jin et al., 2019b). To refine emission inversion processes, innovations like observation bias correction
85 (Jin et al., 2019a), adjoint-based emission source tracking (Jin et al., 2020), and grid adjustment methodologies (Jin et al., 2021) have been introduced, significantly advancing our understanding of dust emission dynamics and their environmental and climatic implications. Despite these advancements, the application of sequential forecasting methodologies utilizing filtering

techniques for dust storms has received limited exploration. To address this gap, we have recently engineered an operational dust forecasting framework that integrates Ensemble Kalman Filter (EnKF) with the LOTOS-EUROS model. This integration is facilitated by our custom assimilation software, Pyfilter (Pang, last access: May, 2024). Testing this system against the backdrop of the record-breaking dust storms of spring 2021 has demonstrated marked improvements in both the assimilated analyses and forecast results compared to standalone model forecasts. Notably, when configured with an appropriate localization radius, it consistently outperformed the EnKF, highlighting the potential for localized filters in enhancing the precision of dust storm forecasting.

Despite the encouraging outcomes of our experimental assessments, several challenges persist, chief among them being a spatial misalignment between model forecast and observations following long-distance dust transport. This disparity not only encompasses discrepancies in the estimated dust intensity but also manifests in inaccuracies regarding the timing of dust arrival and departure, as will be elaborated in Sect. 2.4. In the context of dust storm forecasting evaluation, both the intensity and the position accuracy of the dust plume are paramount. Intensity directly correlates with the amount of airborne dust, while the position is vital for understanding where the dust plume affects at a given instant. For operational forecasting and warning systems, pinpointing the correct location of impending dust impacts can carry even greater urgency than estimating dust load precisely. Quantitatively, these spatial mismatches significantly deteriorate the forecast performance when evaluated using conventional measures like the root mean square error (RMSE). The underlying causes of this spatial discrepancy and its broader ramifications on forecasting efficacy will be meticulously examined in Sect. 3.2.

The phenomenon labeled as "position error" in dust aerosol simulations typically emerges following long-distance transport. This error is multifaceted, stemming from a constellation of factors including the simplification of physical processes in models, coarse spatial and temporal resolutions, indeterminate values of physical parameters (Ravela et al., 2007), and uncertainties inherent to both meteorological inputs and the precise timing of dust emissions, as we previously highlighted (Jin et al., 2021). Resembling the issues encountered in dust emission inversion, discrepancies between model forecast and observations in dust storm data assimilation efforts can also be traced back to uncertainties in dust emission estimates, where ensemble simulations incorporate varied emission scenarios. The challenge lies in the quantification of position error and its subsequent inaccurate formulation of the background error covariance matrix. Consequently, EnKF calibrates both intensity and position error, while it cannot handle position errors if the ensemble is under-dispersive with regard to position. This deficiency curtails the capacity of current assimilation methodologies to correct position error.

Position error is not an occasional issue. Instead, it is a error that accumulates as simulations progress, plaguing forecasts such as hurricanes, dust storms, convective thunderstorms, and precipitation (Dance, 2004; Nehrkorn et al., 2015; Jin et al., 2021). However, efforts explicitly targeting the mitigation of this error have been relatively scarce. One pioneering study by Brewster (2003) outlined an objective methodology to pinpoint and rectify position errors leveraging a wealth of high-resolution, densely deployed observational data. Their findings in Observing System Simulation Experiments (OSSEs) affirmed the feasibility of correcting position errors. Jin et al. (2021) developed a grid distortion strategy grounded in image morphing techniques for post-processing, effectively realigning modeled dust plumes to conform more closely with observations. While these enhancements underscore the potential for addressing position errors, their efficacy hinges critically on the availability of

a comprehensive and closely spaced observational network. Regrettably, in many practical scenarios, observational coverage is patchy and incomplete, curtailing the broad application of these corrective measures.

125 In this paper, the EnKF is coupled with a Valid Time Shifting (VTS) strategy, referred to henceforth as VTS-EnKF, specifically tailored to mitigate position errors prevalent in long-distance dust storm transport. The VTS methodology, inspired by prior works such as Xu et al. (2008); Lu et al. (2011); Zhao et al. (2015); Huang and Wang (2018), augments the EnKF by incorporating temporal flexibility to better align simulated dust plumes with observations. In practice, the VTS-EnKF enhances the background error covariance estimation for each assimilation cycle by considering not solely the immediate ensemble mem-
130 bers but also those from neighboring time points, slightly before and after the target moment (Gasperoni et al., 2022, 2023). By doing so, this approach encapsulates a broader range of potential dust plume positions, thereby inherently compensating for transport-related inaccuracies without necessitating intricate adjustments to observations, meteorological inputs, or other underlying physical parameters. The efficacy of the VTS-EnKF was assessed against two severe dust storm events that occurred in 2021. Our findings underscore the substantial improvement offered by this hybrid method over EnKF, particularly in
135 scenarios where significant position errors are evident in model prior. This advancement paves the way for more precise and temporally coherent dust storm forecasting, especially amidst the complexities of long-distance transport.

This paper is organized as follows: Section 2 introduces the dust measurements and dust model used in the research. We also discuss that the major uncertainty of dust model forecast comes from the emission. But there is another problem: position error that remains to be solved. Then in Sect. 3, we explain introducing the procedure of ensemble-based assimilation algorithm
140 and the mechanism of position error's negative effect on EnKF. How the new assimilation method works is explained in detail afterwards. To test the performance of EnKF with VTS, sequential assimilation experiments on several dust storm events are designed. Section 4 analyses the results of experiments in terms of both the assimilation analysis and forecast performance. Section 5 concludes this paper.

2 Dust observation, model and position error

145 In this paper, ground-based PM_{10} is used as the dust observation to be assimilated after a bias-correction procedure to remove the non-dust part. The dust model adopted is the LOTOS-EUROS. Considering the model processes, the greatest uncertainty in the dust simulation comes from uncertainty the emission parameterization. Meanwhile, uncertainties from meteorology can also influence the model forecast and lead to the "Position error".

2.1 Ground PM_{10} observations

150 Thanks to the continuous efforts and investments from the Ministry of Ecology and Environment, over 1600 ground monitoring stations have been established across China, with some locations in northern China shown in Fig. 1. These stations provide real-time hourly air quality data, and their hourly PM_{10} concentrations serve as indispensable datasets for measuring dust load, which are used as observations to be assimilated in this paper.

Despite the advantages of low uncertainty and high time resolution, PM₁₀ observations are not assimilated directly due to the mixed state of dust and non-dust aerosols in the original PM₁₀ data. Anthropogenic activities, such as vehicle emissions, coal burning, and industrial processes (Wu et al., 2018; Liu et al., 2018), along with natural sources like volcanic eruptions, sea spray, wildfires, and wind-blown dust contribute to the total PM₁₀ concentration. Assimilating PM₁₀ data directly into a dust model may introduce biases and lead to model divergence (Jin et al., 2019a). Therefore, it is necessary to eliminate the bias before data assimilation.

In this study, the non-dust portion of PM₁₀ is approximated through a separate model. The dust observations assimilated are calculated by subtracting the non-dust fraction from the original PM₁₀ measurements. Further details regarding the baseline removal (BR) can be found in Jin et al. (2022).

2.2 Dust model

In this paper, the LOTOS-EUROS v2.1 is used to simulate dust storms that occurred in East Asia. Originating from the Long-Term Ozone Simulation (LOTOS) and the European Operational Smog model (EUROS) in the 1980s, LOTOS-EUROS has undergone continuous development for various applications. It has been widely used in air quality forecasting (Curier et al., 2012; Brasseur et al., 2019; Lopez-Restrepo et al., 2020; Skoulidou et al., 2021), dust/aerosol emission inversion (Yarce Botero et al., 2021; Jin et al., 2018, 2019a, b, 2021, 2022), and source apportionment (Kranenburg et al., 2013; Timmermans et al., 2017; Pommier et al., 2020; Jin et al., 2020). In spring 2021, several super dust storm events occurred in East Asia, around 15th March, 28th March. These events, referred to as DSE1 and DSE2, are used as test cases in this study. These dust storms caused significant losses in both Mongolia and China (Jin, 2021; Chen and Walsh, 2021). Accurate forecast of such severe sandstorms is crucial for reducing health and property damages.

To simulate the dust storm over East Asia, LOTOS-EUROS is configured following our recent work (Jin et al., 2022): The simulation domain is from 15° N to 50° N and 70° E to 140° E with a grid resolution of 0.25° × 0.25°. The model consists of 8 layers with a top at 10 km. The boundary conditions are set to zero assuming that all the dust aerosols are emitted during the simulation window. Dust emission, deposition, advection, diffusion and dry/wet deposition are considered within the model. The model output is at the interval of 1 hour.

The whole model simulation period is set from 13 to 17 March for DSE1 and 27 to 30 March for DSE2, which covering the whole life cycles of emission and long-distance transport. More details could be found in Jin et al. (2022).

2.3 Uncertainties from emission and meteorology

The goal of this study is to calculate the dust concentration field that best fits both the a priori and observations at each assimilation analysis. The optimized field will then be used as the initial condition for sequential dust forecasts, as explained in Section 3.1. It is essential to define and quantify the uncertainty in dust simulations. As previously mentioned, the uncertainty in emission parameterization is widely believed to be the dominant error source in dust simulation (Ginoux et al., 2001, 2012; Di Tomaso et al., 2017, 2022; Jin et al., 2019a, b). High levels of uncertainty in dust emission parameterization arise from insufficient knowledge about windblown erosion, lack of accurate input on soil characteristics, and the models' inability to

resolve the fine-scale variability in wind fields governing dust emission (Escribano et al., 2017; Foroutan et al., 2017; Foroutan and Pleim, 2017; Jin et al., 2019b).

In our recent work (Jin et al., 2022), a 4DVar-based inverse modeling approach was employed to retrieve an optimal emission
 190 field for the three major dust storms in spring 2021 (Jin et al., 2022). The a priori emission, $\mathbf{f}_{\text{priori}}$, followed the *Zender03* dust emission parameterization scheme (Zender et al., 2003). To compensate for potential errors, a spatially varying multiplication factor was introduced. Mathematically, it was quantified by a background error covariance matrix, \mathbf{B} , to describe the potential spread of the actual dust emission flux.

Another source of the uncertainties arises from the meteorological field. In our previous papers, uncertainties from meteo-
 195 rology and the position error were neither taken into account (Jin et al., 2022; Pang et al., 2023). In this paper, European Center for Medium-ranged Weather Forecast (ECMWF) ensemble forecast (totally 51 ensemble members) are used. Each one of the model ensemble members is driven by one unique ensemble meteorology field. Its grid resolution is about 14 km. The 6-hourly short-term meteorological forecast field is interpolated to hourly values and re-gridded to match the model resolution.

In general, we assign the dust simulation uncertainty to both emission and meteorology. Ensemble emission field $[\mathbf{f}_1, \dots, \mathbf{f}_N]$
 200 are generated randomly following the emission uncertainty choice $\mathbf{f}_{\text{priori}}$ and \mathbf{B} in Jin et al. (2022). Meteorologic field $[\mathbf{w}_1, \dots, \mathbf{w}_N]$ are randomly selected from the total 51 ensemble meteorology. They are used to forward the LOTOS-EUROS model \mathcal{M} for the ensemble dust simulations $[\mathbf{x}_1, \dots, \mathbf{x}_N]$ as:

$$[\mathbf{x}_1, \dots, \mathbf{x}_N] = [\mathcal{M}(\mathbf{f}_1, \mathbf{w}_1), \dots, \mathcal{M}(\mathbf{f}_N, \mathbf{w}_N)] \quad (1)$$

N refers to the total ensemble number, and the choice will be explained in Section 3.3.

205 These ensemble individuals are used in the EnKF assimilation for representing the covariance dynamics of the dust plume, which resulted in more accurate dust analysis and forecast as will be shown in Sect. 4. However, the ensemble realizations mainly represent the uncertainty in the intensity feature, and hardly help resolve the positional deviation between the observation and simulation. The presence of position error would give rise to a divergent assimilation analysis as will be illustrated in Sect. 3.1.

210 2.4 Position error

For all the dust events, most of the dust particles were originated from the Mongolia Gobi desert, and carried by the prevailing wind towards southeast. After several thousands of kilometers transport which lasted about one to two days, they finally arrived in the densely-populated northern China.

Position errors are clearly visible in the simulation of two dust events (DSE1 and DSE2). Examples can be best seen in
 215 Fig. 1, which plots the evolution of LOTOS-EUROS simulated surface dust concentration alongside BR-PM₁₀ (BR: non-dust baseline-removed) concentration observations for DSE1 (panel a) and DSE2 (panel c). The corresponding standard deviations from ensemble model simulations and the model-minus-observation differences (absolute values) are also plotted in panel b and panel d. In panel a.1, the model generally simulates a similar shape of the dust plume as indicated by the observations at the first instance, though the dust load intensities differ to some extent. However, during the subsequent transport, positional

220 errors arise gradually. In panel a.2, the right part of the simulated dust plume is positioned about 100 to 200 km too far south compared to ground-based observations. Consequently, the Root Mean Square Error (RMSE) increases significantly from 587.83 $\mu\text{g m}^{-3}$ at 8:00 to 856.36 $\mu\text{g m}^{-3}$ at 11:00. This position error continues to accumulate over the following 3 hours at 14:00. The development of position errors is further clearly visible against the PM_{10} observations, especially in the light blue box in panel a.3. The model simulation missed all the dust load there, while the observations indicate a significant amount
225 of dust aerosols. It can also be seen in panel b.3 that the model-minus-observation differences exceed 1000 $\mu\text{g m}^{-3}$ there. Similarly, for DSE2 occurring on 28th March, 2021, as shown in Fig. 1(c), discrepancies between observations and simulation become more explicit as time evolves, especially for the dust in the light blue box in panels c.1 and c.2. The RMSE remains high from 542.15 $\mu\text{g m}^{-3}$ at 8:00 to 479.6 $\mu\text{g m}^{-3}$ at 11:00, and this error expands to a wider extent as shown in the enlarged green box in panel c.3. This position error not only limits the model forecast performance but also significantly degrades the
230 subsequent assimilation analysis and forecast. With an ensemble-approximated background covariance unrepresentative of position error, neither the position deviation nor the intensity deviation can be fully resolved, as will be explained in Sect. 3.2.

Potential sources of position error in dust model may be attributed to inaccuracies in emission timing, uncertainties in meteorological input data (e.g., wind fields responsible for transporting dust plumes from the Gobi Desert in Mongolia and China to downwind regions), or a combination of these factors. Adjusting the emission timing profile, which characterizes the release
235 of soil particles into the atmosphere, could partially correct the position of the dust plume. Moreover, alterations in meteorological conditions governing long-distance transport might also realign the dust plume's position. To address the position error, a comprehensive covariance matrix is necessary to account for both the potential variations in emission temporal profiles and the accumulation of uncertainties along the plume's extensive trajectory. Concurrently, a significantly larger ensemble size is required to propagate these uncertainties, featuring high degrees of freedom, into the PM_{10} observational space. Although
240 a sophisticated covariance matrix and a substantial ensemble size (resulting in considerable computational cost) may aid the EnKF in simultaneously resolving position and intensity errors, this approach is often prohibitively expensive. Therefore, an efficient and cost-effective alternative solution is required.

3 Assimilation methodology and experiments

EnKF is a powerful algorithm to tune the model simulation with observations especially in intensity adjustment given the
245 perturbed emission spreads. However, when faced with the position error, its weakness is exposed that some model-minus-observation inconsistency cannot be resolved by EnKF as illustrated in Section 3.1. On the contrary, our EnKF with VTS can correct both the position error and the intensity. Assimilation strategy is designed and embedded into a assimilation forecast system in Section 3.2. Experiments are designed on the dust storms occur in spring, 2021, which are illustrated in Section 3.3.

3.1 EnKF

250 The Ensemble Kalman Filter (EnKF) was first proposed by Evensen (1994). Stemming from the Kalman Filter, it was designed to address high-dimensional problems by employing limited ensemble members to approximate the true background error

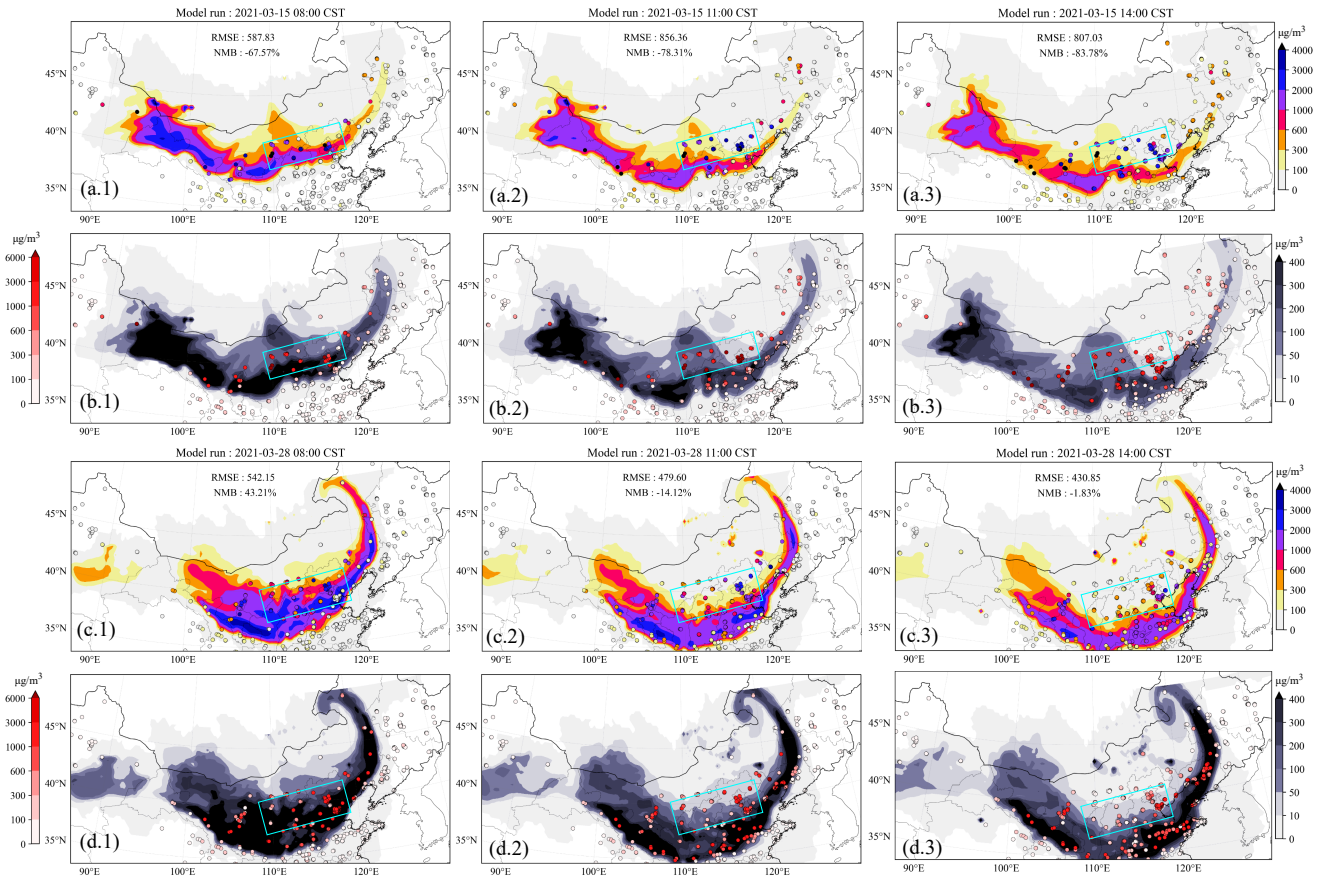


Figure 1. Evolution of the simulated dust plume from average of ensemble members (**a.1-3**). Their corresponding standard deviation from ensemble members (**b.1-3**) at 08:00, 11:00 and 14:00 15th March, 2021, respectively. Figures below are the same except the time is at 05:00 (**c.1** and **d.1**), 08:00 (**c.2** and **d.2**), 11:00 (**c.3** and **d.3**) 28th March, 2021, respectively. The filled circles represent ground BR-PM₁₀ observations in (**a**) and (**c**), and the model-minus-observation differences (absolute value) at various observation sites in (**b**) and (**d**). The colorbar in panel **a** and **c** represents the concentrations, and the colorbar in panel **b** and **d** represents the model-minus-observation differences (left) and standard deviation (right). BR-PM₁₀: baseline-removed PM₁₀. CST: China Standard Time.

covariance. It relies on the Gaussian distribution of errors. The EnKF has been proven to be practical and efficient in various applications, particularly in sequential forecasting with the aid of localization (Lopez-Restrepo et al., 2020; Park et al., 2022). In any sequential forecast system, the objective of assimilation analysis is to provide an optimized initial state or parameter field, which, in this study, corresponds to the 3D dust concentration. This is achieved by assimilating the available measurements. The estimated dust concentration field can then be used to onward the model for more accurate dust forecasting.

Here we use the stochastic EnKF formulated by Burgers et al. (1998). It features the perturbed observations to maintain a reliable ensemble spread. Starting from the prior dust concentration field $\mathbf{x}_t^{f,i}$ at time t which is calculated by model integral operator \mathcal{M} from the dust concentration field at the previous time step $\mathbf{x}_{t-1}^{a,i}$.

$$260 \quad \mathbf{x}_t^{f,i} = \mathcal{M}(\mathbf{x}_{t-1}^{a,i}, \mathbf{f}^i, \mathbf{w}^i) \quad (2)$$

$$\mathbf{X}^f = [\mathbf{x}_t^{f,1}, \mathbf{x}_t^{f,2}, \dots, \mathbf{x}_t^{f,N}] \quad (3)$$

Note that for the first analysis the prior dust simulation are extracted from the model with the perturbed emissions as shown in Eq. 1. The i represents the ensemble individual number. N is the number of ensemble. \mathbf{X}^f is the ensemble model simulation matrix consists of the whole ensemble individuals.

The ensemble perturbation matrix $\mathbf{X}^{f'}$ calculates the deviation between the ensemble individuals $\mathbf{x}_t^{f,i}$ and the ensemble mean state $\bar{\mathbf{x}}_t^f$.

$$\bar{\mathbf{x}}_t^f = \frac{1}{N} \sum_{i=1}^N \mathbf{x}_t^{f,i} \quad (4)$$

$$270 \quad \mathbf{X}^{f'} = [\mathbf{x}_t^{f,1} - \bar{\mathbf{x}}_t^f, \mathbf{x}_t^{f,2} - \bar{\mathbf{x}}_t^f, \dots, \mathbf{x}_t^{f,N} - \bar{\mathbf{x}}_t^f] \quad (5)$$

Then the background error covariance matrix \mathbf{P}^f is approximated by $\mathbf{X}^{f'}$ as follows:

$$\mathbf{P}^f = \frac{1}{N-1} \mathbf{X}^{f'} \mathbf{X}^{f'\top} \quad (6)$$

Afterwards, the Kalman gain \mathbf{K} can be calculated with \mathbf{P}^f and \mathbf{O} .

$$\mathbf{K} = \mathbf{P}^f \mathcal{H}^\top (\mathcal{H} \mathbf{P}^f \mathcal{H}^\top + \mathbf{O})^{-1} \quad (7)$$

\mathbf{K} weights the increments given from the observations to the prior estimation. In this paper, they are the BR-PM₁₀ observations stored in \mathbf{y} and dust simulation stored in vector \mathbf{x} . \mathcal{H} is the observation operator which maps the model states into the observational space.

\mathbf{O} is the observational error covariance matrix that weights the uncertainty of the measurements. In this case, it is the uncertainties from ground-based BR-PM₁₀ concentrations. \mathbf{O} is defined as follows: the minimum uncertainty threshold is set

280 to be $200 \mu\text{g m}^{-3}$. Standard deviation of observation error below the threshold is set to be $200 \mu\text{g m}^{-3}$ and those over it is set to be $200 + (\mathbf{y} - 200) \times 0.2 \mu\text{g m}^{-3}$. This definition can prevent the posteriori from getting too close to the low value observations and thus leading to model divergence. \mathbf{O} is a diagonal matrix assuming that all the observations are independent.

In the end, the posteriori estimation individual $\mathbf{x}_t^{a,i}$ can be updated as follows:

$$\mathbf{x}_t^{a,i} = \mathbf{x}_t^{f,i} + \mathbf{K}(\mathbf{y} + \boldsymbol{\epsilon}^i - \mathcal{H}\mathbf{x}_t^{f,i}) \quad (8)$$

285 $\boldsymbol{\epsilon}^i$ represents the sampling error vector. It is a random vector subjecting to normal distribution. Its mean is 0 and variance is the root of diagonal from \mathbf{O} .

The equations presented above describe the Ensemble Kalman Filter (EnKF) algorithm for dust storm assimilation, which focuses on intensity adjustment. The EnKF assimilation aims to compute an optimal posteriori estimation given a priori information and observations. It is highly dependent on both the observations and the ensemble spread. In fact, the ensemble-based background covariance matrix, \mathbf{P}^f , utilizes the ensemble members to approximate the true background covariance. The performance of EnKF deteriorates when position errors are present. The underlying mechanism can be best understood by examining Fig. 2(a). At time point t_0 , there are ensemble model simulations (gray dashed lines) distributed across the three-dimensional space. The black line and blue star represent the average of model ensemble and observations, respectively. As clearly depicted, there is a positional mismatch between the ensemble model simulations and observations. Following the assimilation analysis, 295 the intensity of the dust plume is adjusted to better match the observations. However, in the spatial domain outside the priori, the dust concentration is reduced to near-zero levels. The observations in this area, containing valuable information about dust load, contribute little to correcting the dust load. This is due to the unanimous agreement on the dust load from the model ensemble, which represents low uncertainty. In such cases, the assimilation analysis favors the model results and disregards the observations. Consequently, the a posteriori estimate is biased as a result of ensemble underdispersion.

300 3.2 VTS-EnKF

To efficiently perform the assimilation analysis with both the intensity and position errors present, we apply a "valid time shifting" method into the EnKF. The strategy is illustrated in Fig. 2(b). Instead of using the ensemble simulations solely at the exact assimilation analysis instant t_0 , as shown in panel a, ensemble members at neighboring moments are also introduced to expand the ensemble group. These resampled ensemble members at neighboring times represent the potential positions of the 305 actual dust plume. The enlarged ensemble exhibit a more extensive spread of the dust plume in the spatial domain compared to those displayed in panel a. The joint ensemble model simulations then capture uncertainty in both intensity and position. The a posteriori estimate (red line) is adjusted to better fit the observations, with both of these errors resolved.

Mathematically, the EnKF with VTS procedures are very similar to those of EnKF, except that the original \mathbf{X}^f is replaced by $\mathbf{X}^{f,new}$, which stores the enlarged ensemble members at the assimilation analysis instant and neighboring times. It starts 310 with

$$\mathbf{X}^{f,new} = [\mathbf{x}_{t-\tau}^{f,1}, \mathbf{x}_{t-\tau}^{f,2}, \dots, \mathbf{x}_{t-\tau}^{f,N}, \mathbf{x}_t^{f,1}, \mathbf{x}_t^{f,2}, \dots, \mathbf{x}_t^{f,N}, \mathbf{x}_{t+\tau}^{f,1}, \mathbf{x}_{t+\tau}^{f,2}, \dots, \mathbf{x}_{t+\tau}^{f,N}] \quad (9)$$

Let t be the exact assimilation time, and τ be the time interval. Then $t - \tau$ represents the time in the past, and $t + \tau$ represents the time in the future. It is noteworthy that the time axis, denoted by $t - \tau$ and $t + \tau$, is utilized solely to illustrate the application of ensemble simulations at different time direction in the formula. However, in practical applications, ensemble members from multiple adjacent time instants can be incorporated, as demonstrated in the horizon choice utilized in this study (as presented in Table 1).

Subsequently, the ensemble-based background covariance \mathbf{P}^f , Kalman gain \mathbf{K} and posteriori state x^a will be updated with the $\mathbf{X}^{f,new}$ in Eq. 6 ~ 8, respectively.

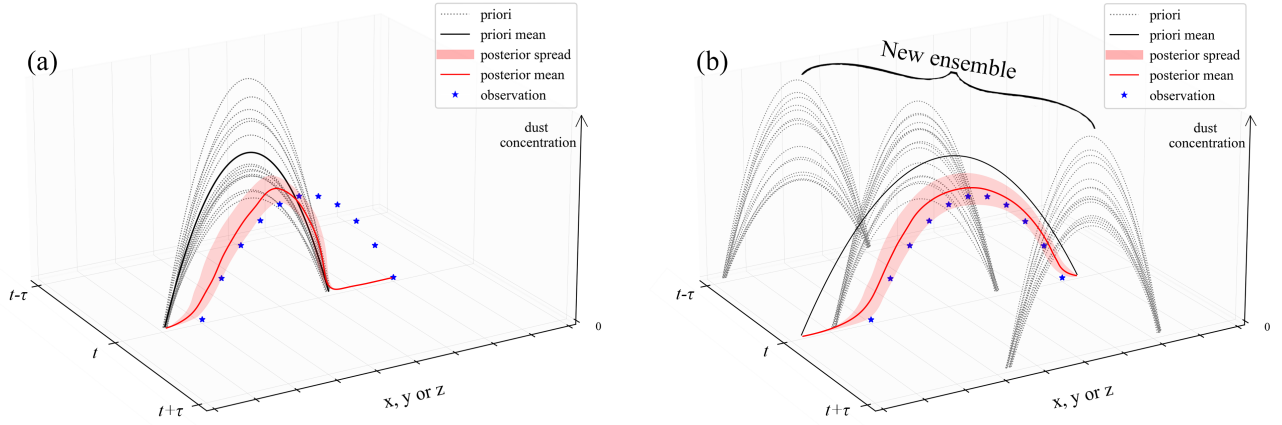


Figure 2. Strategy illustration of ensemble Kalman filter (EnKF) (a) and ensemble Kalman filter with VTS (VTS-EnKF) (b). Figure axis left represents the time and right represents the position of the dust field in 3D space. The vertical axis represents the intensity of the dust.

The localization method is also adopted here to cut off the spurious correlation in \mathbf{P}^f and constrain the background covariance to a certain distance. The localization matrix is constructed following Gaspari and Cohn (1999) (Eq. A.27) with a distance threshold L_{thres} . The details about the construction of \mathbf{L} can be found in Supporting Information. The localized $\mathbf{P}^{f,local}$ is obtained by point to point multiply with localization matrix \mathbf{L} .

$$\mathbf{P}^{f,local} = \mathbf{P}^f \circ \mathbf{L} \quad (10)$$

With the localized $\mathbf{P}^{f,local}$, the localized posteriori estimation $x_t^{a,i}$ can be updated via Eq. 7 and Eq. 8.

Both the EnKF and EnKF with VTS described above are embedded into our self-designed assimilation toolbox, PyFilter (Pang, last access: May, 2024). This toolbox features a flexible interface for linking to numerical models (Pang et al., 2023), such as the dust storm forecasting model LOTOS-EUROS used in this study.

3.3 Experiment descriptions

DSE1 and DSE2 are chosen as the cases for the test. The BC-PM₁₀ observations are assimilated. The first assimilation analysis
330 did not commence until the dust plume was detected by the ground-based observation network and a position mismatch
emerged. An identification index is also designed to objectively discriminate the position error as can be found in Eq. S6
in Supplementary. Three sequential EnKF analyses are conducted in each dust event at three-hour intervals. The timeline for
DSE1 and DSE2 is depicted in Fig. 3.

Taking DSE1 as an example, the initial assimilation analysis is performed at 11:00 March 15, when an apparent position
335 error was present, as illustrated in Fig. 1 (a.2). The last analysis is carried out at 17:00 March 15. As the dust loading decreases
rapidly when the plume moves further southeast, no additional assimilation is performed. A rolling forecast (red line with
arrow) is generated based on the optimized dust concentration field with a 24-hour horizon for the purpose of examining
forecast skill.

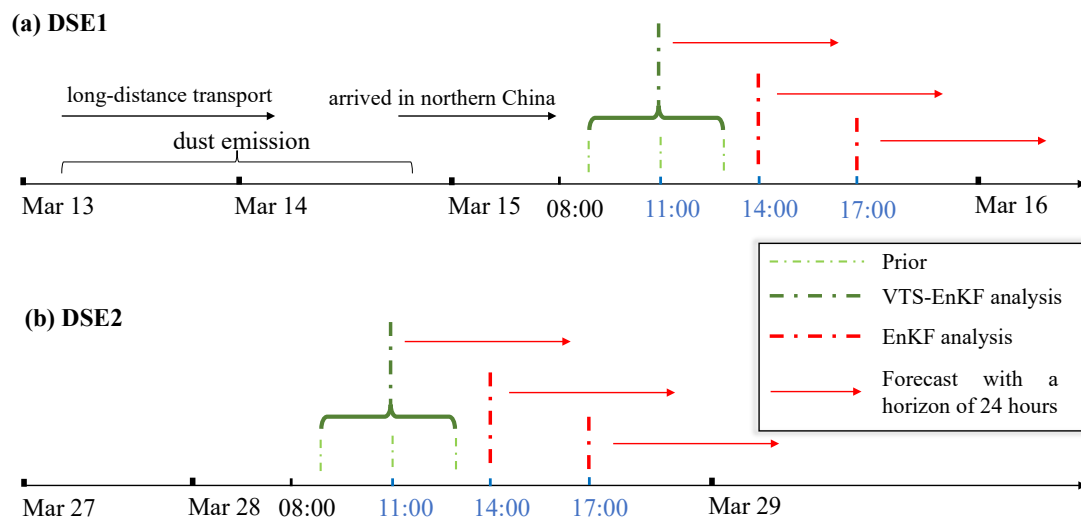


Figure 3. Sequential assimilation time set for DSE1 (a) and DSE2 (b). Take DSE1 for instance, the assimilation analysis is performed at the intervals of 3 hours from 11:00 to 17:00 and the rolling forecast is made with a horizon of 24 hours based on the assimilation analysis. The EnKF with VTS and EnKF is performed in turn.

To evaluate the performance of the VTS-EnKF-implemented dust storm forecasting system, data assimilation experiments
340 are conducted on two spring dust events in 2021. Experiment settings are shown in Table 1. *Control* represents the ensemble

model forecast throughout the entire dust storm period. *Basic* and *L500* denote the assimilation-based forecasts by EnKF and localized EnKF (LEnKF) with a localization distance threshold of 500 km, respectively. *VTS-EnKF* and *VTS-L500* represent the assimilation-based forecasts by VTS-EnKF and VTS-EnKF with a localization distance threshold of 500 km. Note that various distance thresholds have been tested for localization, and a choice of 500 km is found to provide the optimal assimilation analysis and forecast in our tested cases. The metrics, Root Mean Square Error (RMSE) and Normalized Mean Bias (NMB), are employed in this paper to evaluate system performance. Calculation of the metrics is mentioned in supporting information.

In EnKF-based experiments, *Basic* and *L500*, the ensemble number N is set to 32, which is found to be sufficient to represent the uncertainty in the dust simulation while remaining computationally affordable. Testing with N greater than 32 shows only limited improvements. For VTS-EnKF experiments, the ensemble is expanded as they incorporate simulations from neighboring instants. To cover the potential positions of the dust plume, neighboring times with ± 1 and ± 2 hours apart are empirically chosen in this paper. As demonstrated in Table 1, the ensemble number is extended to 160 when EnKF with VTS is applied, and the neighboring time stamps of 9:00, 10:00, 12:00, and 13:00 are selected. The 160 ensemble dust simulations are updated according to the EnKF principles and forwarded synchronously for the new rolling forecast; they will serve as the prior in the subsequent assimilation analysis.

Experiments for the VTS-EnKF with equal ensemble members to EnKF are designed, as referred to *VTS-EnKF-small* and *VTS-L500-small*. They start with central 8 ensemble members and are extended to 32 by incorporating neighboring ± 1 and ± 2 hours with 4×6 ensemble members. Furthermore, to test the sensitivity of neighboring time interval, VTS-EnKF experiments with different intervals are also designed. Time intervals ranging from 1 to 5 hours are selected to test the impact, which are referred to as *VTS-EnKF-t1*, *VTS-EnKF-t2*, *VTS-EnKF-t3*, *VTS-EnKF-t4* and *VTS-EnKF-t5*.

4 Results and discussions

The results are discussed in the aspects of assimilation analysis and model forecast. The benefits of using our EnKF with VTS algorithm for the dust storm simulation with position errors are emphasized.

4.1 Impact on assimilation analysis

There are noticeable position errors arise with the transport of dust storm. It is clearly shown in Fig. 1 (b,d) that the spatial distribution of the standard deviation (square root of the diagonal values in \mathbf{P}^f) from 32 model ensemble members, along with the scatter of absolute model-minus-observation differences in two cases (DSE1, DSE2). In general, their spatial distribution corresponds well to the simulated dust field depicted in Fig. 1 (a, c). Concurrently, the uncertainty in the light blue box decreases rapidly as the simulated dust plume moves southward, as illustrated in panels b.1 and b.2. This suggests that our ensemble model simulations are highly confident that there are less affected by dust aerosols. However, the observations indicate that this area remains heavily polluted. In the case of DSE2, the situation becomes more complex. The simulated dust plume in DSE2 covers most of the observation area with a high dust load, as demonstrated in panels c.1 and d.1. The uncertainty, on the other hand, reveals that the ensemble model is less confident about the dust load, especially in the light blue box displayed in panel d.2.

Table 1. Experiment settings.

Name	Ensemble size used by analysis and forecast	Initial assimilation time set (hour)	Ensemble set	Localization distance (km)
<i>Control</i>	32	None	[32]	None
<i>Basic</i>	32	t	[32]	None
<i>L500</i>	32	t	[32]	500
<i>VTS-EnKF</i>	160	$t - 2, t - 1, t, t + 1, t + 2$	[32,32,32,32,32]	None
<i>VTS-L500</i>	160	$t - 2, t - 1, t, t + 1, t + 2$	[32,32,32,32,32]	500
<i>VTS-EnKF-small</i>	32	$t - 2, t - 1, t, t + 1, t + 2$	[6,6,8,6,6]	None
<i>VTS-L500-small</i>	32	$t - 2, t - 1, t, t + 1, t + 2$	[6,6,8,6,6]	500
<i>VTS-EnKF-t1</i>	96	$t - 1, t, t + 1$	[32,32,32]	None
<i>VTS-EnKF-t2</i>	96	$t - 2, t, t + 2$	[32,32,32]	None
<i>VTS-EnKF-t3</i>	96	$t - 3, t, t + 3$	[32,32,32]	None
<i>VTS-EnKF-t4</i>	96	$t - 4, t, t + 4$	[32,32,32]	None
<i>VTS-EnKF-t5</i>	96	$t - 5, t, t + 5$	[32,32,32]	None
<i>VTS-EnKF-t6</i>	96	$t - 6, t, t + 6$	[32,32,32]	None

After 3 hours, these discrepancies become more evident. The extent to which this situation affects the EnKF assimilation will be discussed in this paper. It poses a challenge to EnKF assimilation in resolving the high-value measurements in this region.

375 Subsequent results have confirmed this theory. Figure 4 displays the spatial distribution of ground BR-PM₁₀ observations (scatter) and dust field forecasts from the average of the ensemble (panel a.1), the posteriori from EnKF analysis (panel a.2) and EnKF with localization (panel a.3), the average of the enlarged ensemble (panel b.1), the posteriori from VTS-EnKF analysis (panel b.2) and VTS-EnKF analysis with localization (panel b.3) at 11:00, 15th March, 2021 China Standard Time (CST). It should be noted that the average dust concentrations in panel b.1 are calculated from the 160 ensemble simulations
380 used in VTS-EnKF, which slightly differ from the average of 32 ensemble members. In DSE1, the RMSE and NMB from the ensemble model simulation are as high as 856.36 $\mu\text{g m}^{-3}$ and -78.31 %. Both EnKF and LEnKF assimilation analyses achieve very limited improvement in estimating the dust state field. As shown in panel a.2 and panel a.3, the RMSE and NMB remain high at 819.04 $\mu\text{g m}^{-3}$ and -75.65 % in *Basic*, and 782.57 $\mu\text{g m}^{-3}$ and -73.52 % in *L500*. The main reason for this is the ensemble underdispersion, as described in Sect. 3.2. As observed in the light blue box in panel a.1, the simulated dust plume is
385 located farther southeast compared to the PM₁₀ measurements. This snapshot exhibits an apparent position error. After EnKF analysis, the simulated dust plume in the light blue box barely changes, as depicted in panel a.2. Numerous ground stations in this area report high PM₁₀ concentrations, but the assimilated dust field fails to resolve most of them. The localization method offers limited assistance in this situation, as illustrated in panel a.3. With the unresolved positional error, the EnKF, which focuses more on intensity correction, is much less effective.

390 When it comes to the VTS-EnKF analysis result, an improved dust field can be noticed. Concerning the Root Mean Square Error (RMSE) and Normalized Mean Bias (NMB), the two priors depicted in panels a.1 and b.1 exhibit highly similar performances. However, slight differences do exist. For instance, the average of the expanded 160-member ensemble used in VTS-EnKF displays a marginally broader spread. The increased ensemble size provides more room for representing background uncertainties. The enhanced capacity for this is best illustrated in Fig. 6 (a), which exhibits the uncertainty quantified by the
395 enlarged ensemble simulations in VTS-EnKF formulations. This expansion of the uncertainty spread effectively addresses the issue of ensemble underdispersion, thereby boosting the EnKF's capability to handle position errors. In contrast, the relatively low uncertainty over these areas depicted in Fig. 1 (b.2) suggests that the EnKF method is highly confident in the absence of aerosols and does not require any modification. The observations are effectively assimilated in the VTS-EnKF analysis. As displayed in panel b.2, the dust plume within the light blue box is adjusted to better match the observations. In particular, the
400 dust to the east of the marked region is well represented in comparison to the posteriori of *Basic*. The RMSE and NMB are reduced to $742.33 \mu\text{g m}^{-3}$ and -68.21% . Moreover, the posteriori of *VTS-L500* yields an improved dust field with the RMSE and NMB further reduced to $696.1 \mu\text{g m}^{-3}$ and -63.93% . The implementation of the localization method eliminates spurious correlations and generates a background error covariance that more accurately describes the model uncertainties. Despite the noticeable improvements achieved in DSE1, the residual errors, as indicated by the RMSE and NMB metrics, remain relatively
405 high. This is mainly due to some observations with extremely high value (exceeding $5000 \mu\text{g m}^{-3}$), which is far higher than the surrounding stations and hard for the EnKF to adapt. In particular, the western extent of the dust plume is covered by the insufficient stations, which results in an inadequate representation of the dust load. By incorporating neighboring ensemble, the dust plume is extended wider. In the future research, assimilating satellite-derived dust optical depth (DOD) observations that have broader coverage may help to better constrain the enlarged ensemble.

410 Figure 5 presents the spatial distribution of ground-based BR-PM₁₀ observations (scatter) and dust concentration forecasts from the average of model ensemble (panel a.1), EnKF (panel a.2), and LEnKF analysis (panel a.3), as well as the average of the enlarged model ensemble (panel b.1), VTS-EnKF (panel b.2), and VTS-EnKF with localization analysis (panel b.3) at 11:00, March 28th, 2021 CST. During this assimilation snapshot in DSE2, the model-simulated dust field is observed to have moved further southeast, as depicted in panel a.1. As illustrated by the light blue box in panel a.1, the model-simulated dust plume
415 missed most of the observations with high PM₁₀ concentrations. Consequently, although the EnKF analysis remains effective in this case, dust in light blue box is nearly unchanged. The RMSE and NMB are reduced to $348.13 \mu\text{g m}^{-3}$ and -45.96% in the *Basic* scenario, with further reductions to $301.38 \mu\text{g m}^{-3}$ and -39.12% when the localization method is employed in the *L500* case.

For the enlarged ensemble, the RMSE and NMB of the priori for *VTS-EnKF* are $433.08 \mu\text{g m}^{-3}$ and -8.93% . With VTS-
420 EnKF assimilation, the RMSE of the posterior further decreases to $246.23 \mu\text{g m}^{-3}$, and the NMB is -31.61% in *VTS-EnKF*. Unlike the *Basic*, the dust plume in light blue box is noticeably optimized to better fit the observations. RMSE and NMB are significantly lower than those obtained with the *Basic*, thanks to the better-scaled background covariance displayed in Fig. 6. Moreover, by incorporating localization, the RMSE and NMB are further reduced to $221.15 \mu\text{g m}^{-3}$ and -27.23% in *VTS-L500*. The dust load within the light blue box (panel b.3) is accurately reproduced within its actual range ($2000 \sim 3000 \mu\text{g m}^{-3}$).

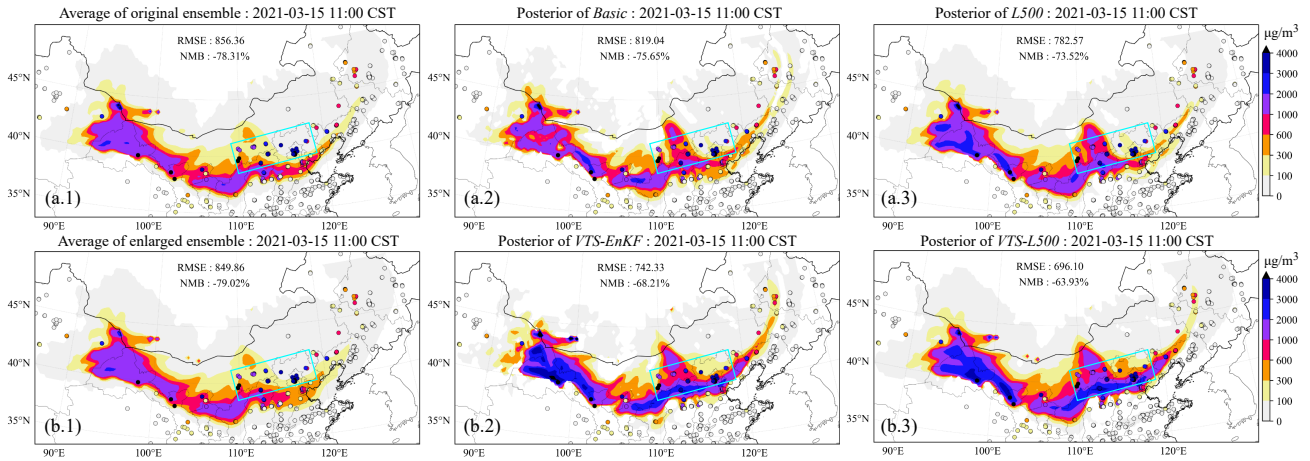


Figure 4. Spatial distribution of simulated dust plume (SDP) on surface from average of ensemble members at central time (a.1), the posteriori SDP updated by EnKF (a.2), the posteriori SDP updated by EnKF with localization (a.3), central and neighboring time ensemble model mean (b.1), the posteriori SDP updated by VTS-EnKF (b.2), the posteriori SDP updated by VTS-EnKF with localization (b.3) at 11:00, 15th March 2021 (CST). The filled circles are ground-based BR-PM₁₀ observations. CST: China Standard Time.

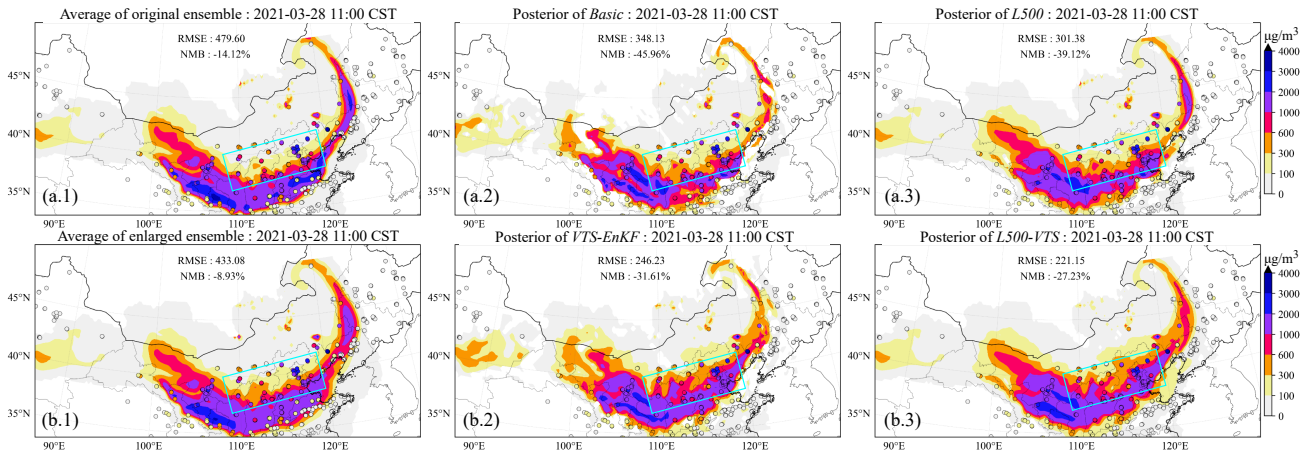


Figure 5. Spatial distribution of simulated dust plume (SDP) on surface from average of ensemble members at central time (a.1), the posteriori SDP updated by EnKF (a.2), the posteriori SDP updated by EnKF with localization (a.3), central and neighboring time ensemble model mean (b.1), the posteriori SDP updated by VTS-EnKF (b.2), the posteriori SDP updated by VTS-EnKF with localization (b.3) at 11:00, 28th March 2021 (CST). The filled circles are ground-based BR-PM₁₀ observations. CST: China Standard Time.

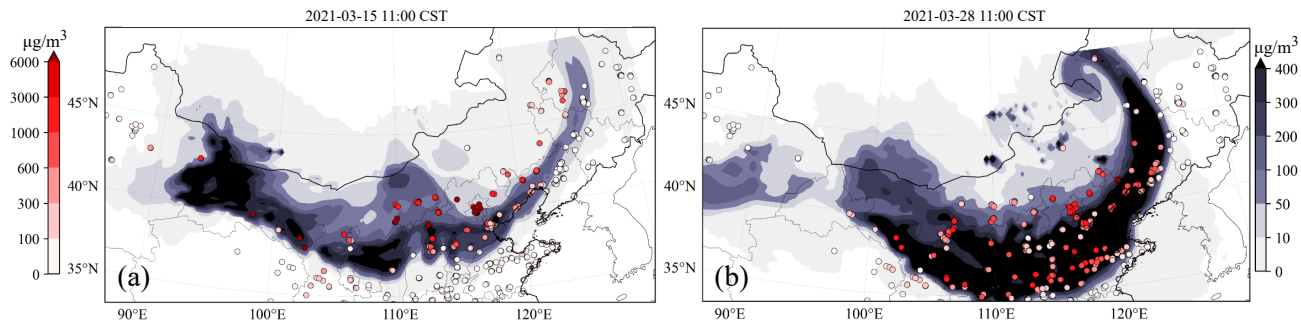


Figure 6. Spatial distribution of standard deviation from ensemble members at 11:00 in DSE1(a) and 08:00 in DSE2(b). The initial assimilation analysis is performed at these time. The filled circles are model-minus-observation differences (absolute value). Colorbar left is for model-minus-observation differences and right is for standard deviation. CST: China Standard Time.

425 4.2 Impact on forecast skills

In addition to the snapshots of the assimilation analysis, an comprehensive evaluation of forecast skills is also necessary to see the performance of VTS-EnKF algorithm. A general evaluation on the forecasting skills is carried out in this section.

Figure 7 presents the time series of RMSE and NMB for the 24-hour dust forecast after three assimilation analyses in DSE1 (starting from 11:00, 14:00, and 17:00). In these cases, the *Control run* generates a dust field with a high RMSE (ranging from
 430 over $800 \mu\text{g m}^{-3}$ to around $600 \mu\text{g m}^{-3}$) and a large NMB (consistently around -85 %). The EnKF analysis, however, does not improve this dust forecast after the initial assimilation. In fact, the RMSE and NMB of the dust forecast from the *Basic* scenario are nearly identical to the *Control run*, as evidenced by the comparison between the black dashed line and the blue line in panel a. This result can be primarily attributed to the position error discussed in Sect. 2.4. The EnKF algorithm offers minimal assistance in correcting the model simulation when position errors are present. These errors are not occasional but
 435 cumulative, as demonstrated in the subsequent two assimilation timestamps at 14:00 and 17:00, during which the assimilation analysis shows limited improvement over the situation. Moreover, it has been observed that the localization method only improves the forecast slightly in the presence of position errors. Similar for NMB, as depicted in panel b, the improvements are also insignificant. The NMB for the *Control*, *Basic*, and *L500* scenarios remains consistently around -85 % throughout the entire forecast time range.

440 By applying the VTS-EnKF analysis, a reduction of RMSE compared to the model run and EnKF can be observed in panel a. There is an approximate decrease of $100 \mu\text{g m}^{-3}$ in *VTS-EnKF* compared to *Basic*, which indicates that the VTS-EnKF analysis effectively corrects the position error. At the subsequent assimilation timestamps, this situation improves, with an even greater decrease in RMSE. The RMSE of *VTS-L500* is slightly lower than that of *VTS-EnKF*. As for NMB, quite promising results are achieved. In *VTS-EnKF*, the NMB decreases stepwise at three time points, from around -75 % at 11:00 to around -70 %
 445 at 14:00, and finally to around -65 %. The VTS-EnKF algorithm gradually takes effect over the three assimilation analyses.

In *VTS-L500*, the localization method demonstrates its efficacy, especially after the third assimilation timestamp at 17:00. The NMB is reduced to around -60 %, which is significantly lower than that of the *L500*.

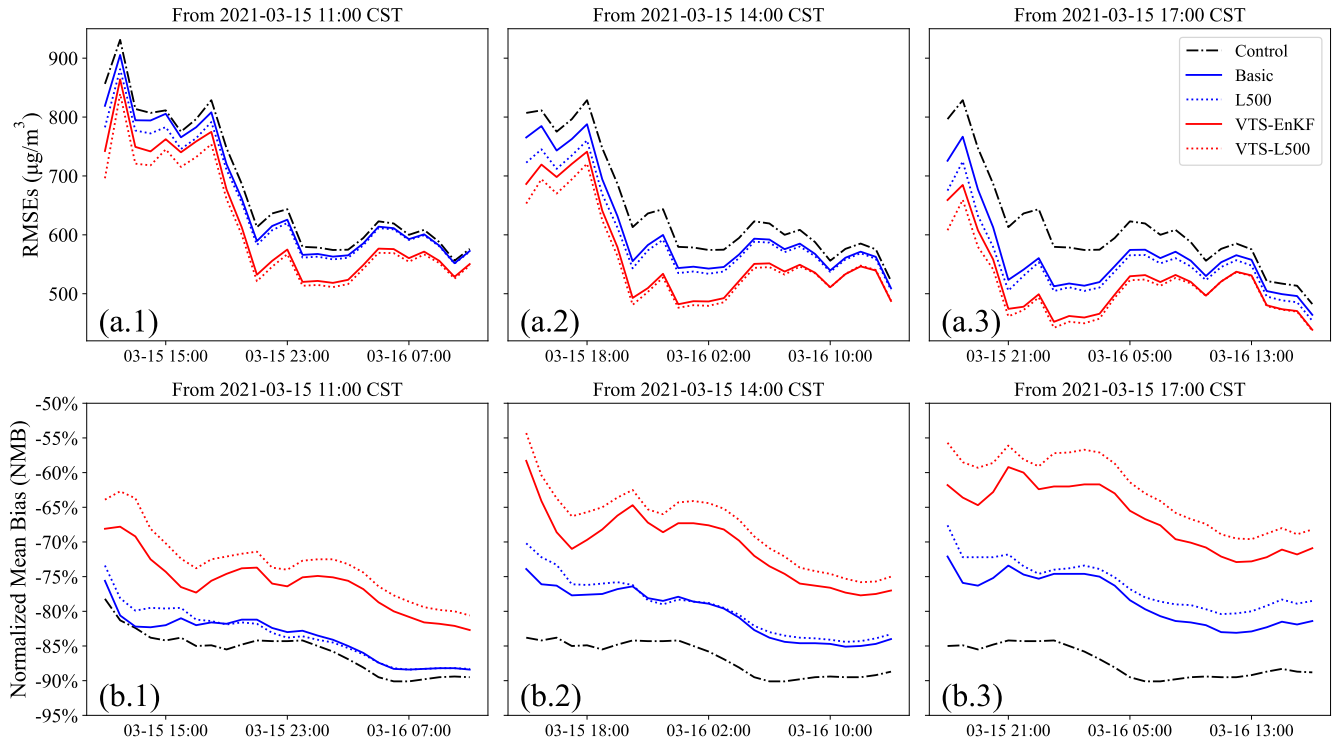


Figure 7. Time series of 24-hour Root Mean Square Error (RMSE) on the dust forecast starting from 11:00 (a.1), 14:00 (a.2), 17:00 (a.3) and normalized mean bias (NMB) starting from 11:00 (b.1), 14:00 (b.2), 17:00 (b.3) on 15th March 2021. CST: China Standard Time.

Figure 8 displays the time series of RMSE and NMB on a 24-hour dust forecast after three assimilation analyses in DSE2. Unlike DSE1, *Basic* in DSE2 does improve the dust forecast in terms of RMSE and NMB. The RMSE drops from around 500 $\mu\text{g m}^{-3}$ to less than 400 $\mu\text{g m}^{-3}$ at the initial assimilation timestamp (11:00). NMB here is higher than *Control* due to the complementary effect of NMB. The overestimation is corrected while the underestimation caused by position error is not corrected. No further reduction is observed at subsequent time points. As can be seen in panels a.2 and a.3, the RMSE of *Basic* remains almost constant compared to panel a.1. This indicates that the position error is not corrected, and it constitutes part of the RMSE that is difficult to eliminate. The trend of NMB also reflects this situation. *L500* is unable to correct the position error, although it does help reduce the error to some extent.

In the scenario of the *VTS-EnKF* analysis, an improvement in the dust forecast of DSE2 is obtained. A general reduction of RMSE (around 50 $\mu\text{g m}^{-3}$) in *VTS-EnKF* compared to *Basic* can be seen in panel a.1. Furthermore, in the subsequent forecasts, a steady decrease in RMSE is noted. The RMSE fluctuates around 250 $\mu\text{g m}^{-3}$ after 14:00 and 200 $\mu\text{g m}^{-3}$ after 17:00. *VTS-L500* exhibits a similar pattern to *VTS-EnKF* for most of the forecast. Considering the NMB, as shown in panel b,

460 the NMB of *VTS-L500* demonstrates trivial superiority over *VTS-EnKF*. In DSE2, the *Basic* and *L500* have already achieved well-reproduced dust fields, while the *VTS-EnKF* and *VTS-L500* can further improve these fields by correcting the position error.

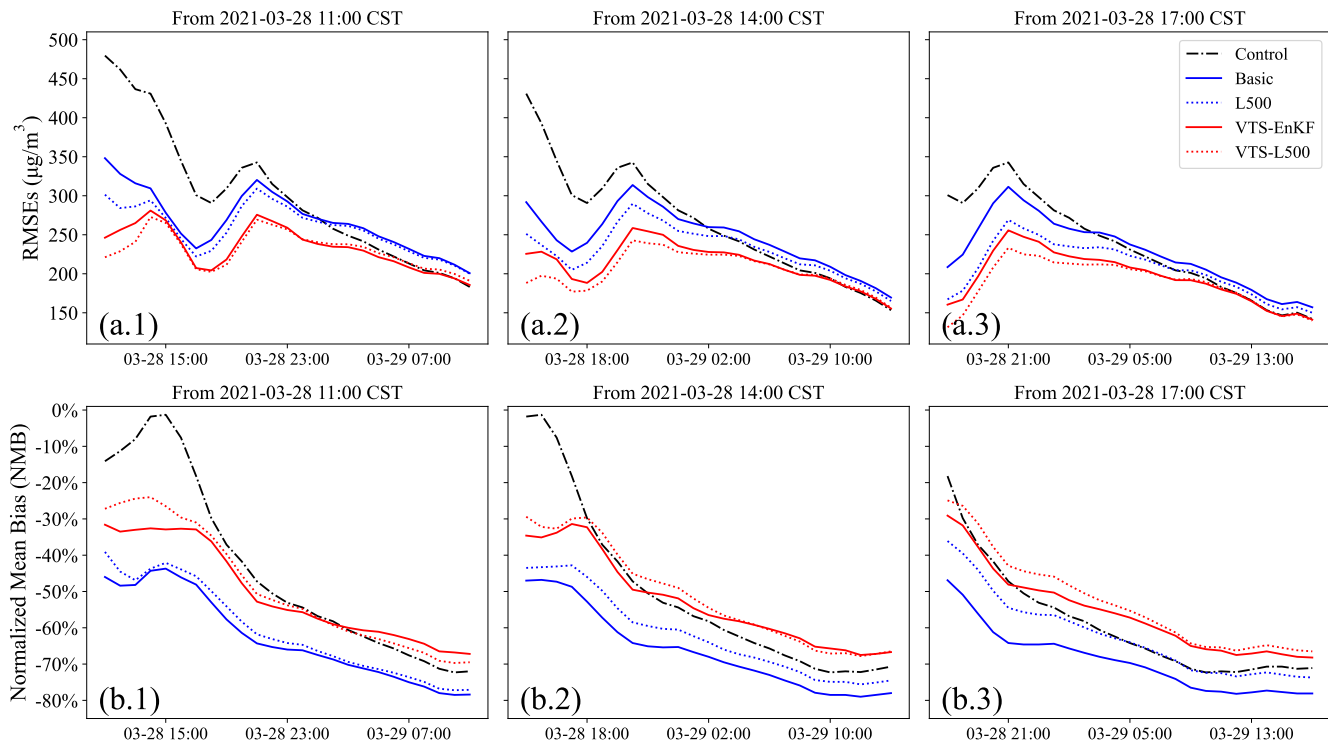


Figure 8. Time series of 24-hour Root Mean Square Error (RMSE) on the dust forecast starting from 08:00 (a.1), 11:00 (a.2), 14:00 (a.3) and normalized mean bias (NMB) starting from 08:00 (b.1), 11:00 (b.2), 15:00 (b.3) on 28th March 2021. CST: China Standard Time.

4.3 Assessment of fewer ensemble members

To further assess the performance of *VTS-EnKF*, *VTS-EnKF* experiments with same ensemble members as the *EnKF* are designed. They are referred to as *VTS-EnKF-small* and *VTS-L500-small*, respectively. These experiments start from 8 ensemble members that are driven by randomly selected emission and meteorology field from the origin ensemble. During the initial assimilation, the extra 4×6 ensemble members from neighboring ± 1 and ± 2 hours are randomly sampled from these 8 ensemble members. The new ensemble comprises 32 members which is equivalent to the origin ensemble number of *Basic*. Figure 9 displays the time series of RMSE and NMB on a 24-hour dust forecast after three assimilation analyses in DSE1. In terms of RMSE, *VTS-EnKF-small* only shows slightly better performance than the *EnKF*. This mostly caused by the sampling error arises from limited ensemble members resampled from the central ensemble (only 8 ensemble members). However, by applying the localization, the RMSE is noticeably reduced by $100 \mu\text{g m}^{-3}$. The performance is comparable to the *VTS-L500* (red

dash line) with totally 160 ensemble members. By mitigating the sampling error, the VTS-EnKF's capability of handling the position error can be revealed, which can be noticed by comparison with *L500* and *VTS-L500-small*. This improvement can be better seen in NMB. NMB of *VTS-L500-small* is much lower than the *Basic* and *L500*. Its performance is also comparable to the *VTS-L500* with 160 ensemble members.

Same experiments on DSE2 are also carried out. Results can be found in Fig. S2 in supporting information. Similar to DSE1, the *VTS-EnKF-small* achieves slightly better RMSE and NMB than *Basic* and *L500*. While in *VTS-L500-small*, noticeable improvements can be found especially for the forecast after the second and last assimilation. Reduction of 100 $\mu\text{g m}^{-3}$ in RMSE and 20% in NMB are obtained.

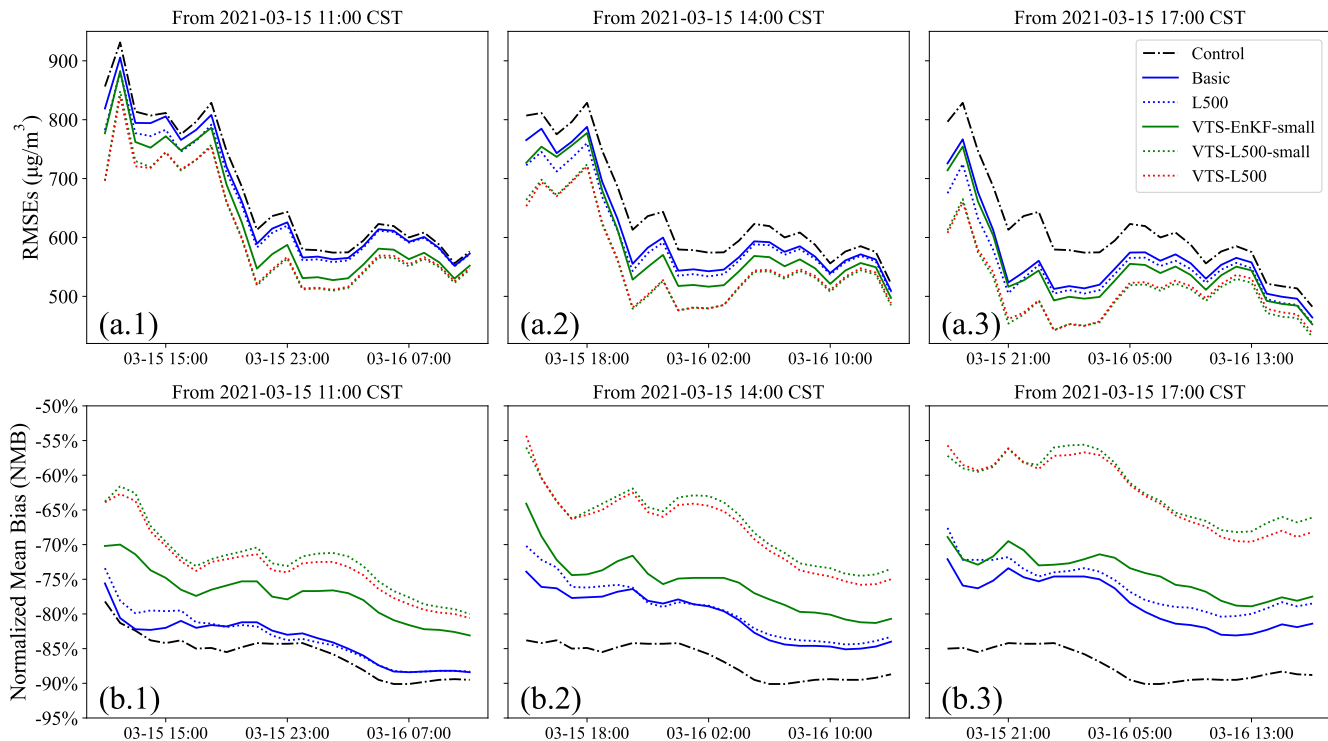


Figure 9. Time series of 24-hour Root Mean Square Error (RMSE) on the dust forecast starting from 11:00 (a.1), 14:00 (a.2), 17:00 (a.3) and normalized mean bias (NMB) starting from 11:00 (b.1), 14:00 (b.2), 17:00 (b.3) on 15th March 2021. CST: China Standard Time.

4.4 Sensitivity of time interval

Previous researches have found that an improper neighboring time interval τ can lead to undesirable results, such as less-effective ensemble members (interval too small) (τ too small) or ensemble member clustering and unrepresentative ensemble covariances (τ too large) (Xu et al., 2008; Gasperoni et al., 2022, 2023). To explore the sensitivity of the choice of neighboring time interval, series of VTS-EnKF experiments with different neighboring time interval were carried out. Time intervals ranging

from 1 to 6 hour were tested. As shown in Fig. 10, snapshots from 6 experiments on DSE1 clearly depicts the trend. In general, all the VTS-EnKF experiments show better performance than EnKF. While in terms of specific time interval, different patterns can be noticed. For short intervals including 1 and 2 hour, there is not sufficient ensemble spread to account for the position error. Thus there are still position error remaining and RMSE is still high. For long intervals including 5 and 6 hour, dust plume is clustered away from central dust plume. Three dust branches are noticed in *VTS-EnKF-t5* and an overly backwards dust plume is noticed in *VTS-EnKF-t6*. In this case, 3-hour interval is the best choice with the lowest RMSE ($696.11 \mu\text{g m}^{-3}$) and NMB (-63.5%).

Same experiments on DSE2 are also performed and snapshots are shown in Fig. S3. Similar patterns are found on DSE2. Lowest RMSE and NMB are achieved in *VTS-EnKF-t4*. Too short interval leads to inability in position error correction and too long interval leads to excessive dust plume. Considering both cases, 3-hour interval is the preferred choice which holds the capability to handle position and not creates excessive clustered dust plume.

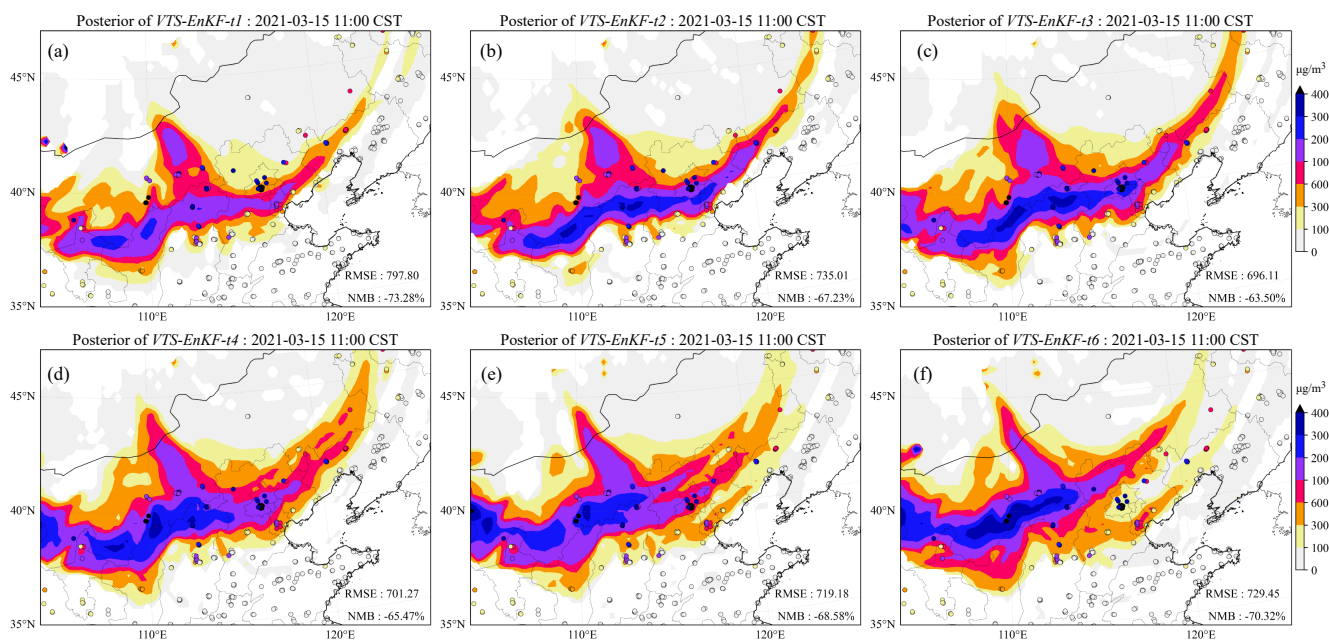


Figure 10. Spatial distribution of ground-based BR-PM₁₀ observations (scatter) and simulated dust plume (SDP) on surface from the posteriori SDP updated by *VTS-EnKF-t1* (a), the posteriori SDP updated by *VTS-EnKF-t2* (b), the posteriori SDP updated by *VTS-EnKF-t3* (c), the posteriori SDP updated by *VTS-EnKF-t4* (d), the posteriori SDP updated by *VTS-EnKF-t5* (e), the posteriori SDP updated by *VTS-EnKF-t6* (f) at 11:00, 15th March 2021 (CST).

5 Conclusions

The Chemistry Transport Model (CTM) is a powerful tool for air pollutant forecasting. However, as a simplified version of the real atmospheric world, it suffers from various deficiencies, particularly in two major uncertainties: emissions and meteorology. Uncertainty from meteorological fields can cause model forecast errors, especially in long-distance transport. In dust storm forecasting applications, a position error is noted that significantly degrades the overall performance of the forecast and prevents the EnKF assimilation algorithm from effectively incorporating observational data.

The background error covariance of EnKF is generally designed to represent the intensity and position uncertainty. However, when the position error is sufficiently large, the background error covariance can't adequately represent the position error, which is highly non-Gaussian. In the case of the long-distance dust storm tracking, the EnKF is incapable of thoroughly resolving the observations. Observations over low model uncertainty pixels are 'ignored' by the EnKF algorithm. To address this issue, a valid time shifting method is coupled with EnKF. This VTS-EnKF methodology introduces uncertainty of the dust plume position into the background error covariance by incorporating extra ensemble simulations at neighboring time instances. This enlarged ensemble not only reflects the uncertainty of dust intensity but also reveals the potential positions of the plume, allowing for more accurate and effective assimilation and improving dust storm forecasting.

The VTS-EnKF algorithm was tested on two super dust storm events (DSE1 and DSE2) that occurred in Spring 2021. Several experiments were designed to examine the performance of the VTS-EnKF algorithm in these cases, with a focus on differences between EnKF and VTS-EnKF. In terms of assimilation analysis, the VTS-EnKF analysis corrected the position error in DSE1 to a large extent. Comparison between the standard deviations from posterior of EnKF and VTS-EnKF explained for it. The standard deviations from VTS-EnKF analysis indicated wilder potential dust spread and were more consistent with the model-minus-observation. Observations that were 'ignored' by EnKF were comprehensively resolved in VTS-EnKF, resulting in decreased RMSE and NMB. For DSE2, the position error was not as significant as in DSE1; however, ensemble underdispersion were also observed. Nevertheless, VTS-EnKF still produced an improved dust field with lower RMSE and NMB compared to EnKF. In both cases, the localization method helped reduce RMSE and NMB. Regarding the forecast performance, promising results were obtained. In DSE1, the RMSE and NMB revealed that EnKF provides limited improvements compared to model run. In contrast, VTS-EnKF provided a dust field forecast with reduced errors, especially in terms of NMB. Additionally, the localization method contributed to further reducing the error. Overall, the VTS-EnKF algorithm demonstrated improved performance in assimilation analysis and forecasting for the tested dust storm events compared to the traditional EnKF approach.

Assessment of equal ensemble members between EnKF and VTS-EnKF is carried out. VTS-EnKF with smaller ensemble size shows slightly improved metrics than EnKF. While by applying localization, more reduction in RMSE and NMB can be noticed and its performance is comparable to the VTS-EnKF with larger ensemble size. This is due to the corrected sampling error within limited ensemble members. Comparison between them confirms VTS-EnKF's ability in handling position error. Sensitivity of neighboring time interval choice is also examined. Too short interval leads to inability in position error correction and too long interval leads to excessive dust plume. Considering both cases, 3-hour interval is the preferred choice.

Code and data availability. The EnKF with VTS code is archived on Zenodo at <https://doi.org/10.5281/zenodo.7611976> (Pang, last access: May, 2024). The PM₁₀ data used in this study is also archived on Zenodo at <https://doi.org/10.5281/zenodo.6459866> (Jin, 2022). The real-time PM₁₀ data established by the Ministry of Ecology and Environment is available to the public at <https://quotsoft.net/air> (Wang, last access: May, 2024). The source code and user guide of the LOTOS-EUROS model could be obtained from <https://lotos-euros.tno.nl> (TNO, last access: May 2024).

Author contributions. JJ conceived the study and designed VTS-EnKF algorithm. MP wrote the code of the assimilation and carried out the experiments and evaluation. AS, HJ, WH, BB, JX, LF, JL, HXL and HL provided useful comments on the paper. MP and JJ prepared the manuscript with contributions from HJ and all others co-authors.

Acknowledgements. This work is supported by the National Natural Science Foundation of China [grant No. 42105109 and 42205031] and Natural Science Foundation of Jiangsu Province (No. BK20210664).

Competing interests

The authors declare that they have no conflict of interest.

References

- Amezcuca, J. and Van Leeuwen, P. J.: Gaussian Anamorphosis in the Analysis Step of the EnKF: A Joint State-Variable/Observation Approach, *TELLUS A*, 66, 23 493, <https://doi.org/10.3402/tellusa.v66.23493>, 2014.
- An, L., Che, H., Xue, M., Zhang, T., Wang, H., Wang, Y., Zhou, C., Zhao, H., Gui, K., Zheng, Y., Sun, T., Liang, Y., Sun, E., Zhang, H., and Zhang, X.: Temporal and Spatial Variations in Sand and Dust Storm Events in East Asia from 2007 to 2016: Relationships with Surface Conditions and Climate Change, *Sci. Total Environ.*, 633, 452–462, <https://doi.org/10.1016/j.scitotenv.2018.03.068>, 2018.
- Bannister, R. N.: A Review of Operational Methods of Variational and Ensemble-Variational Data Assimilation, *Q. J. R. Meteorolog. Soc.*, 143, 607–633, <https://doi.org/10.1002/qj.2982>, 2017.
- Bergamaschi, P., Krol, M., Meirink, J. F., Dentener, F., Segers, A., van Aardenne, J., Monni, S., Vermeulen, A. T., Schmidt, M., Ramonet, M., Yver, C., Meinhardt, F., Nisbet, E. G., Fisher, R. E., O’Doherty, S., and Dlugokencky, E. J.: Inverse Modeling of European CH₄ Emissions 2001–2006, *J. Geophys. Res.*, 115, D22 309, <https://doi.org/10.1029/2010JD014180>, 2010.
- Brasseur, G. P., Xie, Y., Petersen, A. K., Bouarar, I., Flemming, J., Gauss, M., Jiang, F., Kouznetsov, R., Kranenburg, R., Mijling, B., Peuch, V.-H., Pommier, M., Segers, A., Sofiev, M., Timmermans, R., van der A, R., Walters, S., Xu, J., and Zhou, G.: Ensemble Forecasts of Air Quality in Eastern China – Part 1: Model Description and Implementation of the MarcoPolo–Panda Prediction System, Version 1, *Geosci. Model Dev.*, 12, 33–67, <https://doi.org/10.5194/gmd-12-33-2019>, 2019.
- Brewster, K. A.: Phase-Correcting Data Assimilation and Application to Storm-Scale Numerical Weather Prediction. Part I: Method Description and Simulation Testing, *Mon. Weather Rev.*, 131, 480–492, [https://doi.org/10.1175/1520-0493\(2003\)131<0480:PCDAAA>2.0.CO;2](https://doi.org/10.1175/1520-0493(2003)131<0480:PCDAAA>2.0.CO;2), 2003.
- Brunner, D., Henne, S., Keller, C. A., Reimann, S., Vollmer, M. K., O’Doherty, S., and Maione, M.: An Extended Kalman-filter for Regional Scale Inverse Emission Estimation, *Atmos. Chem. Phys.*, 12, 3455–3478, <https://doi.org/10.5194/acp-12-3455-2012>, 2012.
- Burgers, G., Jan van Leeuwen, P., and Evensen, G.: Analysis Scheme in the Ensemble Kalman Filter, *Mon. Weather Rev.*, 126, 1719–1724, [https://doi.org/10.1175/1520-0493\(1998\)126<1719:ASITEK>2.0.CO;2](https://doi.org/10.1175/1520-0493(1998)126<1719:ASITEK>2.0.CO;2), 1998.
- Chen, L. and Walsh, M.: Vast Sandstorms Expose Mongolia’s Long-Ignored Ecological Crisis, 2021.
- Corazza, M., Bergamaschi, P., Vermeulen, A. T., Aalto, T., Haszpra, L., Meinhardt, F., O’Doherty, S., Thompson, R., Moncrieff, J., Popa, E., Steinbacher, M., Jordan, A., Dlugokencky, E., Brühl, C., Krol, M., and Dentener, F.: Inverse Modelling of European N₂O Emissions: Assimilating Observations from Different Networks, *Atmos. Chem. Phys.*, 11, 2381–2398, <https://doi.org/10.5194/acp-11-2381-2011>, 2011.
- Curier, R., Timmermans, R., Calabretta-Jongen, S., Eskes, H., Segers, A., Swart, D., and Schaap, M.: Improving Ozone Forecasts over Europe by Synergistic Use of the LOTOS-EUROS Chemical Transport Model and in-Situ Measurements, *Atmos. Environ.*, 60, 217–226, <https://doi.org/10.1016/j.atmosenv.2012.06.017>, 2012.
- Dance, S. L.: Issues in High Resolution Limited Area Data Assimilation for Quantitative Precipitation Forecasting, *Physica D*, 196, 1–27, <https://doi.org/10.1016/j.physd.2004.05.001>, 2004.
- Di Tomaso, E., Schutgens, N. A. J., Jorba, O., and Pérez García-Pando, C.: Assimilation of MODIS Dark Target and Deep Blue Observations in the Dust Aerosol Component of NMMB-MONARCH Version 1.0, *Geosci. Model Dev.*, 10, 1107–1129, <https://doi.org/10.5194/gmd-10-1107-2017>, 2017.
- Di Tomaso, E., Escribano, J., Basart, S., Ginoux, P., Macchia, F., Barnaba, F., Benincasa, F., Bretonnière, P.-A., Buñuel, A., Castrillo, M., Cuevas, E., Formenti, P., Gonçalves, M., Jorba, O., Klose, M., Mona, L., Montané Pinto, G., Mytilinaios, M., Obiso, V., Olid, M.,

- 580 Schutgens, N., Votsis, A., Werner, E., and Pérez García-Pando, C.: The MONARCH High-Resolution Reanalysis of Desert Dust Aerosol over Northern Africa, the Middle East and Europe (2007–2016), *Earth Syst. Sci. Data*, 14, 2785–2816, <https://doi.org/10.5194/essd-14-2785-2022>, 2022.
- Duncan Fairlie, T., Jacob, D. J., and Park, R. J.: The Impact of Transpacific Transport of Mineral Dust in the United States, *Atmos. Environ.*, 41, 1251–1266, <https://doi.org/10.1016/j.atmosenv.2006.09.048>, 2007.
- 585 Escribano, J., Boucher, O., Chevallier, F., and Huneus, N.: Impact of the Choice of the Satellite Aerosol Optical Depth Product in a Sub-Regional Dust Emission Inversion, *Atmos. Chem. Phys.*, 17, 7111–7126, <https://doi.org/10.5194/acp-17-7111-2017>, 2017.
- Evensen, G.: Sequential Data Assimilation with a Nonlinear Quasi-Geostrophic Model Using Monte Carlo Methods to Forecast Error Statistics, *J. Geophys. Res.*, 99, 10 143, <https://doi.org/10.1029/94JC00572>, 1994.
- Filonchik, M. and Peterson, M.: Development, Progression, and Impact on Urban Air Quality of the Dust Storm in Asia in March 15–18, 2021, *Urban Clim.*, 41, 101 080, <https://doi.org/10.1016/j.uclim.2021.101080>, 2022.
- 590 Foroutan, H. and Pleim, J. E.: Improving the Simulation of Convective Dust Storms in Regional-to-Global Models, *J. Adv. Model. Earth Syst.*, 9, 2046–2060, <https://doi.org/10.1002/2017MS000953>, 2017.
- Foroutan, H., Young, J., Napelenok, S., Ran, L., Appel, K. W., Gilliam, R. C., and Pleim, J. E.: Development and Evaluation of a Physics-Based Windblown Dust Emission Scheme Implemented in the CMAQ Modeling System, *J. Adv. Model. Earth Syst.*, 9, 585–608, <https://doi.org/10.1002/2016MS000823>, 2017.
- 595 Gaspari, G. and Cohn, S. E.: Construction of Correlation Functions in Two and Three Dimensions, *Q. J. R. Meteorolog. Soc.*, 125, 723–757, <https://doi.org/10.1002/qj.49712555417>, 1999.
- Gasperoni, N. A., Wang, X., and Wang, Y.: Using a Cost-Effective Approach to Increase Background Ensemble Member Size within the GSI-Based EnVar System for Improved Radar Analyses and Forecasts of Convective Systems, *Mon. Weather Rev.*, 150, 667–689, <https://doi.org/10.1175/MWR-D-21-0148.1>, 2022.
- 600 Gasperoni, N. A., Wang, X., and Wang, Y.: Valid Time Shifting for an Experimental RRFS Convection-Allowing EnVar Data Assimilation and Forecast System: Description and Systematic Evaluation in Real Time, *Mon. Weather Rev.*, 151, 1229–1245, <https://doi.org/10.1175/MWR-D-22-0089.1>, 2023.
- Ginoux, P., Chin, M., Tegen, I., Prospero, J. M., Holben, B., Dubovik, O., and Lin, S.-J.: Sources and Distributions of Dust Aerosols Simulated with the GOCART Model, *J. Geophys. Res.*, 106, 20 255–20 273, <https://doi.org/10.1029/2000JD000053>, 2001.
- 605 Ginoux, P., Prospero, J. M., Gill, T. E., Hsu, N. C., and Zhao, M.: Global-Scale Attribution of Anthropogenic and Natural Dust Sources and Their Emission Rates Based on MODIS Deep Blue Aerosol Products, *Rev. Geophys.*, 50, <https://doi.org/10.1029/2012RG000388>, 2012.
- Gong, S. L. and Zhang, X. Y.: CUACE/Dust – an Integrated System of Observation and Modeling Systems for Operational Dust Forecasting in Asia, *Atmos. Chem. Phys.*, 8, 2333–2340, <https://doi.org/10.5194/acp-8-2333-2008>, 2008.
- 610 Goudie, A. S.: Desert Dust and Human Health Disorders, *Environ. Int.*, 63, 101–113, <https://doi.org/10.1016/j.envint.2013.10.011>, 2014.
- Gross, J. E., Carlos, W. G., Dela Cruz, C. S., Harber, P., and Jamil, S.: Sand and Dust Storms: Acute Exposure and Threats to Respiratory Health, *AM J RESP CRIT CARE*, 198, P13–P14, <https://doi.org/10.1164/rccm.1987P13>, 2018.
- Gui, K., Yao, W., Che, H., An, L., Zheng, Y., Li, L., Zhao, H., Zhang, L., Zhong, J., Wang, Y., and Zhang, X.: Record-Breaking Dust Loading during Two Mega Dust Storm Events over Northern China in March 2021: Aerosol Optical and Radiative Properties and Meteorological Drivers, *Atmos. Chem. Phys.*, 22, 7905–7932, <https://doi.org/10.5194/acp-22-7905-2022>, 2022.
- 615 Hamill, T. M.: Ensemble-Based Atmospheric Data Assimilation, in: *Predictability of Weather and Climate*, edited by Palmer, T. and Hagedorn, R., pp. 124–156, Cambridge University Press, 1 edn., <https://doi.org/10.1017/CBO9780511617652.007>, 2006.

- Houtekamer, P. L. and Zhang, F.: Review of the Ensemble Kalman Filter for Atmospheric Data Assimilation, *Mon. Weather Rev.*, 144, 4489–4532, <https://doi.org/10.1175/MWR-D-15-0440.1>, 2016.
- 620 Houtekamer, P. L., Mitchell, H. L., Pellerin, G., Buehner, M., Charron, M., Spacek, L., and Hansen, B.: Atmospheric Data Assimilation with an Ensemble Kalman Filter: Results with Real Observations, *Mon. Weather Rev.*, 133, 604–620, <https://doi.org/10.1175/MWR-2864.1>, 2005.
- Houtekamer, P. L., Deng, X., Mitchell, H. L., Baek, S.-J., and Gagnon, N.: Higher Resolution in an Operational Ensemble Kalman Filter, *Mon. Weather Rev.*, 142, 1143–1162, <https://doi.org/10.1175/MWR-D-13-00138.1>, 2014.
- 625 Hu, Z., Huang, J., Zhao, C., Bi, J., Jin, Q., Qian, Y., Leung, L. R., Feng, T., Chen, S., and Ma, J.: Modeling the Contributions of Northern Hemisphere Dust Sources to Dust Outflow from East Asia, *Atmos. Environ.*, 202, 234–243, <https://doi.org/10.1016/j.atmosenv.2019.01.022>, 2019.
- Huang, B. and Wang, X.: On the Use of Cost-Effective Valid-Time-Shifting (VTS) Method to Increase Ensemble Size in the GFS Hybrid 4DVar System, *Mon. Weather Rev.*, 146, 2973–2998, <https://doi.org/10.1175/MWR-D-18-0009.1>, 2018.
- 630 Jin, G.: The Most Severe Sandstorm in a Decade, 2021.
- Jin, J.: Ground-Based Air Quality Measurements during the 2021 Spring Super Dust Storms, <https://doi.org/10.5281/zenodo.6459866>, 2022.
- Jin, J., Lin, H. X., Heemink, A., and Segers, A.: Spatially Varying Parameter Estimation for Dust Emissions Using Reduced-Tangent-Linearization 4DVar, *Atmos. Environ.*, 187, 358–373, <https://doi.org/10.1016/j.atmosenv.2018.05.060>, 2018.
- Jin, J., Lin, H. X., Segers, A., Xie, Y., and Heemink, A.: Machine Learning for Observation Bias Correction with Application to Dust Storm
635 Data Assimilation, *Atmos. Chem. Phys.*, 19, 10 009–10 026, <https://doi.org/10.5194/acp-19-10009-2019>, 2019a.
- Jin, J., Segers, A., Heemink, A., Yoshida, M., Han, W., and Lin, H.-X.: Dust Emission Inversion Using Himawari-8 AODs Over East Asia: An Extreme Dust Event in May 2017, *J. Adv. Model. Earth Syst.*, 11, 446–467, <https://doi.org/10.1029/2018MS001491>, 2019b.
- Jin, J., Segers, A., Liao, H., Heemink, A., Kranenburg, R., and Lin, H. X.: Source Backtracking for Dust Storm Emission Inversion Using an Adjoint Method: Case Study of Northeast China, *Atmos. Chem. Phys.*, 20, 15 207–15 225, <https://doi.org/10.5194/acp-20-15207-2020>,
640 2020.
- Jin, J., Segers, A., Lin, H. X., Henzing, B., Wang, X., Heemink, A., and Liao, H.: Position Correction in Dust Storm Forecasting Using LOTOS-EUROS v2.1: Grid-Distorted Data Assimilation v1.0, *Geosci. Model Dev.*, 14, 5607–5622, <https://doi.org/10.5194/gmd-14-5607-2021>, 2021.
- Jin, J., Pang, M., Segers, A., Han, W., Fang, L., Li, B., Feng, H., Lin, H. X., and Liao, H.: Inverse Modeling of the 2021 Spring Super Dust
645 Storms in East Asia, *Atmos. Chem. Phys.*, 22, 6393–6410, <https://doi.org/10.5194/acp-22-6393-2022>, 2022.
- Kalman, R. E.: A New Approach to Linear Filtering and Prediction Problems, *J. Basic Eng.*, 82, 35–45, <https://doi.org/10.1115/1.3662552>, 1960.
- Katzfuss, M., Stroud, J. R., and Wikle, C. K.: Understanding the Ensemble Kalman Filter, *The American Statistician*, 70, 350–357, <https://doi.org/10.1080/00031305.2016.1141709>, 2016.
- 650 Kok, J. F., Mahowald, N. M., Fratini, G., Gillies, J. A., Ishizuka, M., Leys, J. F., Mikami, M., Park, M.-S., Park, S.-U., Van Pelt, R. S., and Zobeck, T. M.: An Improved Dust Emission Model – Part 1: Model Description and Comparison against Measurements, *Atmos. Chem. Phys.*, 14, 13 023–13 041, <https://doi.org/10.5194/acp-14-13023-2014>, 2014.
- Kranenburg, R., Segers, A. J., Hendriks, C., and Schaap, M.: Source Apportionment Using LOTOS-EUROS: Module Description and Evaluation, *Geosci. Model Dev.*, 6, 721–733, <https://doi.org/10.5194/gmd-6-721-2013>, 2013.

- 655 Law, K. J. H. and Stuart, A. M.: Evaluating Data Assimilation Algorithms, *Mon. Weather Rev.*, 140, 3757–3782, <https://doi.org/10.1175/MWR-D-11-00257.1>, 2012.
- Leeuwen, P. J., Künsch, H. R., Nerger, L., Potthast, R., and Reich, S.: Particle Filters for High-dimensional Geoscience Applications: A Review, *Q. J. R. Meteorolog. Soc.*, 145, 2335–2365, <https://doi.org/10.1002/qj.3551>, 2019.
- Lei, J., Bickel, P., and Snyder, C.: Comparison of Ensemble Kalman Filters under Non-Gaussianity, *Mon. Weather Rev.*, 138, 1293–1306, <https://doi.org/10.1175/2009MWR3133.1>, 2010.
- 660 Liu, Y., Xing, J., Wang, S., Fu, X., and Zheng, H.: Source-Specific Speciation Profiles of PM_{2.5} for Heavy Metals and Their Anthropogenic Emissions in China, *Environ. Pollut.*, 239, 544–553, <https://doi.org/10.1016/j.envpol.2018.04.047>, 2018.
- Lopez-Restrepo, S., Yarce, A., Pinel, N., Quintero, O., Segers, A., and Heemink, A.: Forecasting PM₁₀ and PM_{2.5} in the Aburrá Valley (Medellín, Colombia) via EnKF Based Data Assimilation, *Atmos. Environ.*, 232, 117 507, <https://doi.org/10.1016/j.atmosenv.2020.117507>, 2020.
- 665 Lu, H., Xu, Q., Yao, M., and Gao, S.: Time-Expanded Sampling for Ensemble-Based Filters: Assimilation Experiments with Real Radar Observations, *Adv. Atmos. Sci.*, 28, 743–757, <https://doi.org/10.1007/s00376-010-0021-4>, 2011.
- Mallet, V. and Sportisse, B.: Uncertainty in a Chemistry-Transport Model Due to Physical Parameterizations and Numerical Approximations: An Ensemble Approach Applied to Ozone Modeling, *J. Geophys. Res.*, 111, <https://doi.org/10.1029/2005JD006149>, 2006.
- Manders, A. M. M., Builtjes, P. J. H., Curier, L., Denier van der Gon, H. A. C., Hendriks, C., Jonkers, S., Kranenburg, R., Kuenen, J. J. P., Segers, A. J., Timmermans, R. M. A., Visschedijk, A. J. H., Wichink Kruit, R. J., van Pul, W. A. J., Sauter, F. J., van der Swaluw, E., Swart, D. P. J., Douros, J., Eskes, H., van Meijgaard, E., van Ulft, B., van Velthoven, P., Banzhaf, S., Mues, A. C., Stern, R., Fu, G., Lu, S., Heemink, A., van Velzen, N., and Schaap, M.: Curriculum Vitae of the LOTOS–EUROS (v2.0) Chemistry Transport Model, *Geosci. Model Dev.*, 10, 4145–4173, <https://doi.org/10.5194/gmd-10-4145-2017>, 2017.
- Marticorena, B. and Bergametti, G.: Modeling the Atmospheric Dust Cycle: 1. Design of a Soil-Derived Dust Emission Scheme, *J. Geophys. Res.*, 100, 16 415, <https://doi.org/10.1029/95JD00690>, 1995.
- 675 Mona, L., Papagiannopoulos, N., Basart, S., Baldasano, J., Biniotoglou, I., Cornacchia, C., and Pappalardo, G.: EARLINET Dust Observations vs. BSC-DREAM8b Modeled Profiles: 12-Year-Long Systematic Comparison at Potenza, Italy, *Atmos. Chem. Phys.*, 14, 8781–8793, <https://doi.org/10.5194/acp-14-8781-2014>, 2014.
- Muhammad Akhlaq, Sheltami, T. R., and Mouftah, H. T.: A Review of Techniques and Technologies for Sand and Dust Storm Detection, *Rev. Environ. Sci. Bio.*, 11, 305–322, <https://doi.org/10.1007/s11157-012-9282-y>, 2012.
- 680 Nehr Korn, T., Woods, B. K., Hoffman, R. N., and Auligné, T.: Correcting for Position Errors in Variational Data Assimilation, *Mon. Weather Rev.*, 143, 1368–1381, <https://doi.org/10.1175/MWR-D-14-00127.1>, 2015.
- Pang, M.: Source Code of PyFilter, Zenodo, <https://doi.org/10.5281/zenodo.7611976>, last access: May. 2024.
- Pang, M., Jin, J., Segers, A., Jiang, H., Fang, L., Lin, H. X., and Liao, H.: Dust Storm Forecasting through Coupling LOTOS-EUROS with Localized Ensemble Kalman Filter, *Atmos. Environ.*, 306, 119 831, <https://doi.org/10.1016/j.atmosenv.2023.119831>, 2023.
- 685 Park, S.-Y., Dash, U. K., Yu, J., Yumimoto, K., Uno, I., and Song, C. H.: Implementation of an Ensemble Kalman Filter in the Community Multiscale Air Quality Model (CMAQ Model v5.1) for Data Assimilation of Ground-Level PM_{2.5}, *Geosci. Model Dev.*, 15, 2773–2790, <https://doi.org/10.5194/gmd-15-2773-2022>, 2022.
- Pérez, C., Nickovic, S., Baldasano, J. M., Sicard, M., Rocadenbosch, F., and Cachorro, V. E.: A Long Saharan Dust Event over the Western Mediterranean: Lidar, Sun Photometer Observations, and Regional Dust Modeling, *J. Geophys. Res.*, 111, D15 214, <https://doi.org/10.1029/2005JD006579>, 2006.
- 690

- Pommier, M., Fagerli, H., Schulz, M., Valdebenito, A., Kranenburg, R., and Schaap, M.: Prediction of Source Contributions to Urban Background PM₁₀ Concentrations in European Cities: A Case Study for an Episode in December 2016 Using EMEP/MSC-W Rv4.15 and LOTOS-EUROS v2.0 – Part 1: The Country Contributions, *Geosci. Model Dev.*, 13, 1787–1807, <https://doi.org/10.5194/gmd-13-1787-2020>, 2020.
- 695 Rabier, F. and Liu, Z.: Variational Data Assimilation: Theory and Overview, in: Proc. ECMWF Seminar on Recent Developments in Data Assimilation for Atmosphere and Ocean, Reading, UK, September 8–12, pp. 29–43, 2003.
- Ravela, S., Emanuel, K., and McLaughlin, D.: Data Assimilation by Field Alignment, *Physica D*, 230, 127–145, <https://doi.org/10.1016/j.physd.2006.09.035>, 2007.
- 700 Reichle, R. H., McLaughlin, D. B., and Entekhabi, D.: Hydrologic Data Assimilation with the Ensemble Kalman Filter, *Mon. Weather Rev.*, 130, 103–114, [https://doi.org/10.1175/1520-0493\(2002\)130<0103:HDAWTE>2.0.CO;2](https://doi.org/10.1175/1520-0493(2002)130<0103:HDAWTE>2.0.CO;2), 2002.
- Shao, Y.: Simplification of a Dust Emission Scheme and Comparison with Data, *J. Geophys. Res.*, 109, D10 202, <https://doi.org/10.1029/2003JD004372>, 2004.
- Shao, Y., Raupach, M., and Leys, J.: A Model for Predicting Aeolian Sand Drift and Dust Entrainment on Scales from Paddock to Region, *Soil Res.*, 34, 309, <https://doi.org/10.1071/SR9960309>, 1996.
- 705 She, L., Xue, Y., Guang, J., Che, Y., Fan, C., Li, Y., and Xie, Y.: Towards a Comprehensive View of Dust Events from Multiple Satellite and Ground Measurements: Exemplified by the May 2017 East Asian Dust Storm, *Nat. Hazards Earth Syst. Sci.*, 18, 3187–3201, <https://doi.org/10.5194/nhess-18-3187-2018>, 2018.
- Skoulidou, I., Koukouli, M.-E., Manders, A., Segers, A., Karagiozidis, D., Gratsea, M., Balis, D., Bais, A., Gerasopoulos, E., Stavrakou, T., van Geffen, J., Eskes, H., and Richter, A.: Evaluation of the LOTOS-EUROS NO₂ Simulations Using Ground-Based Measurements and S5P/TROPOMI Observations over Greece, *Atmos. Chem. Phys.*, 21, 5269–5288, <https://doi.org/10.5194/acp-21-5269-2021>, 2021.
- 710 Song, L., Bi, X., Zhang, Z., Li, L., Dai, Q., Zhang, W., Li, H., Wang, X., Liang, D., and Feng, Y.: Impact of Sand and Dust Storms on the Atmospheric Environment and Its Source in Tianjin-China, *Sci. Total Environ.*, 825, 153 980, <https://doi.org/10.1016/j.scitotenv.2022.153980>, 2022.
- 715 Tang, W., Dai, T., Cheng, Y., Wang, S., and Liu, Y.: A Study of a Severe Spring Dust Event in 2021 over East Asia with WRF-Chem and Multiple Platforms of Observations, *Remote Sens.*, 14, 3795, <https://doi.org/10.3390/rs14153795>, 2022.
- Timmermans, R., Kranenburg, R., Manders, A., Hendriks, C., Segers, A., Dammers, E., Zhang, Q., Wang, L., Liu, Z., Zeng, L., Denier van der Gon, H., and Schaap, M.: Source Apportionment of PM_{2.5} across China Using LOTOS-EUROS, *Atmos. Environ.*, 164, 370–386, <https://doi.org/10.1016/j.atmosenv.2017.06.003>, 2017.
- 720 TNO: Source Code and User Guidance of LOTOS-EUROS, TNO, last access: May 2024.
- Wang, X.: Historical data on air quality in china, <https://quotsoft.net/air/>, last access: May. 2024.
- Wu, X., Vu, T. V., Shi, Z., Harrison, R. M., Liu, D., and Cen, K.: Characterization and Source Apportionment of Carbonaceous PM_{2.5} Particles in China - A Review, *Atmos. Environ.*, 189, 187–212, <https://doi.org/10.1016/j.atmosenv.2018.06.025>, 2018.
- Xu, Q., Wei, L., Lu, H., Qiu, C., and Zhao, Q.: Time-Expanded Sampling for Ensemble-Based Filters: Assimilation Experiments with a Shallow-Water Equation Model, *J. Geophys. Res.*, 113, <https://doi.org/10.1029/2007JD008624>, 2008.
- 725 Yarce Botero, A., Lopez-Restrepo, S., Pínel Peláez, N., Quintero, O. L., Segers, A., and Heemink, A. W.: Estimating NO_x LOTOS-EUROS CTM Emission Parameters over the Northwest of South America through 4DnVar TROPOMI NO₂ Assimilation, *Atmosphere-Basel*, 12, 1633, <https://doi.org/10.3390/atmos12121633>, 2021.

- Yumimoto, K. and Takemura, T.: Long-Term Inverse Modeling of Asian Dust: Interannual Variations of Its Emission, Transport, Deposition, and Radiative Forcing, *J. Geophys. Res. Atmos.*, 120, 1582–1607, <https://doi.org/10.1002/2014JD022390>, 2015.
- 730 Zender, C. S., Bian, H., and Newman, D.: Mineral Dust Entrainment and Deposition (DEAD) Model: Description and 1990s Dust Climatology, *J. Geophys. Res.*, 108, <https://doi.org/10.1029/2002JD002775>, 2003.
- Zhang, R., Arimoto, R., An, J., Yabuki, S., and Sun, J.: Ground Observations of a Strong Dust Storm in Beijing in March 2002, *J. Geophys. Res.*, 110, <https://doi.org/10.1029/2004JD004589>, 2005.
- 735 Zhao, Q., Xu, Q., Jin, Y., McLay, J., and Reynolds, C.: Time-Expanded Sampling for Ensemble-Based Data Assimilation Applied to Conventional and Satellite Observations, *Weather Forecasting*, 30, 855–872, <https://doi.org/10.1175/WAF-D-14-00108.1>, 2015.